



The X-ray emissivity of low-density stellar populations

C. O. Heinke^{1,2} M. G. Ivanov,¹ E. W. Koch¹ R. Andrews,¹ L. Chomiuk,² H. N. Cohn,³ S. Crothers,¹ T. de Boer,⁴ N. Ivanova¹ A. K. H. Kong,⁵ N. W. C. Leigh,^{1,6,7} P. M. Lugger,³ L. Nelson,⁸ C. J. Parr,¹ E. W. Rosolowsky¹ A. J. Ruiter¹ C. L. Sarazin,¹⁰ A. W. Shaw¹ G. R. Sivakoff¹ and M. van den Berg¹²

Affiliations are listed at the end of the paper

Accepted 2020 January 19. Received 2020 January 17; in original form 2018 December 6

ABSTRACT

The dynamical production of low-mass X-ray binaries and brighter cataclysmic variables (CVs) in dense globular clusters is well-established. We investigate how the X-ray emissivity of fainter X-ray binaries (principally CVs and coronally active binaries) varies between different environments. We compile calculations (largely from the literature) of the X-ray emissivity of old stellar populations, including open and globular clusters and several galaxies. We investigate three literature claims of unusual X-ray sources in low-density stellar populations. We show that a suggested quiescent neutron star in the open cluster NGC 6819 is a foreground M dwarf. We show that the suggested diffuse X-ray emission from an old nova shell in the globular cluster NGC 6366 is actually a background galaxy cluster. And we show that a suggested population of quiescent X-ray binaries in the Sculptor Dwarf Galaxy is mostly (perhaps entirely) background galaxies. We find that above densities of $10^4 M_\odot \text{ pc}^{-3}$, the X-ray emissivity of globular clusters increases, due to dynamical production of X-ray emitting systems. Below this density, globular clusters have lower X-ray emissivity than the other populations, and we do not see a strong dependence of X-ray emissivity due to density effects. We find significant correlations between X-ray emissivity and binary fraction, metallicity, and density. Sampling these fits via bootstrap techniques gives less significant correlations, but confirms the effect of metallicity on low-density populations, and that of density on the full globular cluster sample.

Key words: binaries: general – globular clusters: general – open clusters and associations: general – galaxies: stellar content – X-rays: binaries.

1 INTRODUCTION

The effects of dynamical processes in dense environments on X-ray emitting binaries were recognized early in X-ray astronomy (Clark 1975; Katz 1975). It is now well understood that the high densities in the core of globular clusters permit various interactions that place single neutron stars (and black holes) into close binaries, elevating the number of low-mass X-ray binaries (LMXBs) per unit mass in globular clusters to ~ 100 times the Galactic field rate (Fabian, Pringle & Rees 1975; Hills 1976; Verbunt 1987; Hut, Murphy & Verbunt 1991). Studies of the distribution of bright ($L_X > 10^{36} \text{ ergs s}^{-1}$) LMXBs in Galactic and extragalactic globular clusters versus the characteristics of those clusters essentially confirm the theoretically

expected dependence upon cluster dynamical properties (Verbunt & Hut 1987; Jordán et al. 2004; Sivakoff et al. 2007), while also identifying a metallicity dependence (Kundu et al. 2003; Sarazin et al. 2003). Observations of Galactic globular clusters identify roughly ten times as many quiescent LMXB candidates (soft, blackbody-like X-ray sources with $L_X \sim 10^{32-33} \text{ ergs s}^{-1}$) as bright LMXBs (Heinke et al. 2003a; Pooley et al. 2003). The quiescent LMXBs are thought to be transient LMXBs observed between outbursts (e.g. Verbunt, Elson & van Paradijs 1984; Campana et al. 1998). Their numbers in globular clusters clearly show the predicted dependence on cluster properties (Heinke et al. 2006b; Pooley & Hut 2006). Radio millisecond pulsars (MSPs), the progeny of LMXBs, are also distributed among clusters roughly as expected by the theory of collision rates (Johnston, Kulkarni & Phinney 1992; Ransom et al. 2005; Bahramian et al. 2013; Lorimer et al. 2015), though their X-ray luminosities are rarely high enough to dominate the cluster L_X (e.g. Bogdanov et al. 2006; but cf. Becker et al. 2003).

* E-mail: heinke@ualberta.ca (COH); mivanov@ualberta.ca (MGI)

† ARC Future Fellow

With the capabilities of *Hubble* and *Chandra* to identify low-luminosity X-ray sources in dense clusters, it is possible to study the relation between dynamical processes and fainter X-ray emitting binaries. Observations of the numbers of faint ($L_X < 10^{33.5}$ ergs s $^{-1}$) X-ray sources versus globular cluster properties indicate that the brightest such sources, largely cataclysmic variables (CVs) containing white dwarfs (WDs), are more frequent in denser clusters (Johnston & Verbunt 1996; Heinke et al. 2003a; Pooley et al. 2003; Bahramian et al. 2013), though the dependence on cluster density may be less steep than for LMXBs (Heinke et al. 2006b; Pooley & Hut 2006). Theoretical work (Davies 1997; Ivanova et al. 2006; Shara & Hurley 2006; Hong et al. 2017) indicates that dynamical effects both destroy primordial CVs and produce new, dynamically formed CVs, with some work suggesting that CVs are rarer in medium-density globular clusters than in the field due to binary destruction (Shara & Hurley 2006; Belloni et al. 2019). This last prediction has received support from a deep study of ω Centauri's X-ray sources (Haggard, Cool & Davies 2009), which limited the number of CVs in the core of ω Centauri to $< 1/2$ the number expected from field CV density measurements (Patterson 1998; Schwope et al. 2002; Grindlay et al. 2005; Pretorius et al. 2007).

Coronally active binaries (ABs) are (typically) tidally locked partially convective stars, with rotation rates (and thus magnetic fields, and X-ray activity) enhanced over other stars of similar ages. They make up the majority of X-ray sources by number in old stellar populations, though their X-ray luminosities are low (typically $L_X < 10^{31.5}$ ergs s $^{-1}$; Dempsey et al. 1993, 1997). They have been detected in many globular clusters, and have generally been thought to be primordial in origin and their numbers to scale simply with cluster mass (Grindlay et al. 2001; Verbunt 2003; Bassa et al. 2004; Kong et al. 2006). Studies of nearby, moderate-density clusters including M4 and M71 indicate that they have more ABs than expected for their masses, compared to denser globular clusters (Bassa et al. 2004; Elsner et al. 2008; Huang et al. 2010). Several studies have shown that X-rays from lower-density globular clusters are likely dominated by ABs of primordial origin, rather than by dynamically formed binaries (Kong et al. 2006; Bassa et al. 2008; Verbunt, Pooley & Bassa 2008; Lu et al. 2011; Cheng et al. 2018).

Substantial work has been done to identify the nature of the X-ray sources in open clusters, particularly M67 (Belloni, Verbunt & Schmitt 1993; Belloni, Verbunt & Mathieu 1998; van den Berg et al. 2002, 2004), identifying many ABs in close binaries (1–10 d), one CV, and several long-period (30–10⁴ d) binaries whose X-rays cannot be satisfactorily explained. Verbunt (2000, 2001) noted from *ROSAT* observations that globular clusters contain fewer ABs per unit mass than open clusters such as M67; in fact, the total X-ray luminosity per unit mass was lower in most globular clusters without bright LMXBs than in M67. Verbunt suggested two possible explanations: that binaries are destroyed efficiently in globular clusters, and/or that M67 has lost a very large fraction of its mass (and of its non-binary content), thus concentrating X-ray luminous ABs. A key point of this paper is to address this question observationally, by considering the X-ray luminosity per unit mass in a range of environments of different stellar densities. We take advantage of a series of studies establishing the X-ray emissivity of a variety of old stellar populations (Sazonov et al. 2006; Revnivtsev et al. 2007, 2008; Warwick 2014; Ge et al. 2015).

The question of binary destruction in dense environments versus variations in the initial binary fraction in different environments has been a topic of substantial work. Binaries with binding energy less than the typical thermal energy of stellar systems ('soft' binaries; in massive globular clusters, typically these have separations larger

than an AU) are easily destroyed early in clusters' lives (Heggie 1975; Kroupa, Aarseth & Hurley 2001; Parker et al. 2009). Observationally, dense clusters are found to have much lower photometric binary fractions than low-density globular clusters (Bellazzini et al. 2002; Clark, Sandquist & Bolte 2004; Zhao & Bailyn 2005; Sollima et al. 2007; Davis et al. 2008; Milone et al. 2008; Sommariva et al. 2009; Milone et al. 2012), and open clusters are found to have even higher binary fractions (Sollima et al. 2010). Studies have disagreed over whether the fraction of binaries in cluster cores diminishes over time in dense clusters or grows with time (Ivanova et al. 2005; Hurley, Aarseth & Shara 2007), with newer studies giving more complex answers, depending on how soft binaries are treated and whether binaries containing two compact objects are included (Sollima 2008; Fregeau, Ivanova & Rasio 2009).

In this paper, we combine information from the literature and new analyses to compare the X-ray emissivity (X-ray luminosity per unit mass) from a variety of stellar populations, and investigate possible trends with density, metallicity, binary fraction, and age. In Section 2, we compute X-ray luminosities per unit mass for various stellar environments. Then in Section 3, we investigate in detail three particular claims of intriguing objects in relatively low-density stellar systems, where the nature of the object(s) is crucial for our results. In Section 4, we identify a density regime where dynamical production of X-ray binaries dominates X-ray emissivity, and then investigate the effects of metallicity, binary fraction, and age within the lower density regime, where dynamical production of X-ray binaries is not dominant. In Section 5, we compare our results to some recent literature on this topic, and conclude in Section 6.

2 CALCULATIONS OF X-RAY EMISSIVITIES

Here we compute X-ray luminosities per unit mass for a variety of stellar environments. We calculate all X-ray luminosities per unit mass in the 0.5–2.0 keV band, and exclude luminous LMXBs (with $L_X(0.3\text{--}8 \text{ keV}) > 10^{36}$ ergs s $^{-1}$). Where possible we work with values from the literature. We also obtain (typically from the literature) a variety of other quantities that may be relevant to understanding the X-ray emissivity of each population; the metallicity, age, binary fraction, and stellar density of each population. Binary fractions are defined as $f_b = N_b/(N_s + N_b)$, where N_s is the number of single stars, and N_b is the number of binary systems (we include higher order multiples within binaries).

We consider the relevant density in each case to be the highest density which typical binaries will have experienced for a significant fraction (e.g. > 1 Gyr) of their lives. In standard King-model globular clusters, this will be the central (core) density, as typical clusters have relaxed, allowing binaries to segregate into the cluster core. The density experienced by binaries in core-collapsed globular clusters is likely to have a complex history. For these clusters, we also use the standard central density; this choice does not have a large effect on our results, as such clusters are few in number and are the highest density systems. Below we give some details about the values we used for some of these stellar populations.

2.1 Galaxies

We use estimates of the X-ray emissivity of local space (near the Sun), the bulge of M31, the giant elliptical NGC 3379, and the dwarf ellipticals M32, NGC 147, NGC 185, and NGC 205. Galaxies typically have relaxation times longer than the Hubble time, and thus the density we consider is the density of the region where the binaries are found, and presumably were formed. We compute the

Table 1. Properties of non-globular cluster populations.

Name	Distance (kpc)	ρ_c ($M_\odot \text{pc}^{-3}$)	Mass (M_\odot)	Age (Gyr)	Binary Fraction	[Fe/H]	L_X/M ($10^{27} \text{ erg s}^{-1} M_\odot^{-1}$)
Local	<1	0.10	–	5* ± 3	0.44 ± 0.02	-0.15* ± 0.1	9 ± 3
NGC 2682/M67	0.82	32	2100 ± 600	4	0.227 ± 0.021	0.05 ± 0.02	45 ± 14
NGC 188	1.70 ± 0.07	9	2300 ± 460	5.5–7.1	0.29 ± 0.03	-0.03 ± 0.04	25 ± 6
NGC 6791	4.1	11	6000 ± 1000	8–9	0.32 ± 0.03	0.47 ± 0.12	35 ± 8
NGC 6819	2.34 ± 0.06	54	2600	2–2.4	0.22 ± 0.03	-0.02 ± 0.02	37 ± 20
Cr 261	2.45 ± 0.25	15	6500 ± 700	6–7	–	-0.16 ± 0.13	30 ± 7
NGC 185	617	–	1.6×10^8	8–12	–	-1.3 ± 0.1	6.1 ± 2.5
NGC 147	676	–	1.1×10^8	7–13	–	-1.1 ± 0.1	11.2 ± 6.4
NGC 205	824	–	6.8×10^8	9–13	–	-0.8 ± 0.2	7.3 ± 3.8
M31 bulge	780	–	4×10^{10}	6–13	–	-2–0.5	7.5 ± 2
NGC 221/M32	794	1.0*	2.1×10^9	8*(2–10)	–	-0.3* (-0.5–0)	5.4 ± 1.7
NGC 3379	9800	–	5.7×10^{10}	8–10	–	0.3	5.2 ± 1.6

Notes. Properties of non-globular cluster stellar populations considered. Density indicates central densities for open clusters, density of considered region in galaxies. L_X measured in 0.5–2 keV band. L_X/M for open clusters uses $M/2$, since only X-ray sources within the half-mass radius are included. * indicates the average value (for stellar populations showing a range in a parameter).

References: Local: density, Holmberg & Flynn (2000), age and [Fe/H], Nordström et al. (2004), binary fraction, Raghavan et al. (2010), L_X/M , Sazonov et al. (2006), Warwick (2014); M67: mass and binary fraction, Geller et al. (2015), age, Bellini et al. (2010), [Fe/H], Jacobson, Pilachowski & Friel (2011), density, Hurley et al. (2005), L_X/M , van den Berg et al. (2004); NGC 188: mass, Geller et al. (2008), binary fraction, Geller et al. (2015), age and distance Meibom et al. (2009), [Fe/H], Jacobson et al. (2011), L_X/M , Vats et al. (2018); NGC 6791: mass, Platais et al. (2011), age, Grundahl et al. (2008), binary fraction, Bedin et al. (2008), [Fe/H], Gratton et al. (2006), Carraro et al. (2006), L_X/M , van den Berg et al. (2013); NGC 6819: mass Kalirai et al. (2001), age, Basu et al. (2011), binary fraction Milliman et al. (2014), [Fe/H], Lee-Brown et al. (2015), L_X/M , Gosnell et al. (2012), Platais et al. (2013); Collinder 261: age, Bragaglia & Tosi (2006), [Fe/H], Friel et al. (2002), mass & L_X/M , Vats & van den Berg (2017); NGC 185, NGC 147, NGC 205: L_X/M , Ge et al. (2015), others McConnachie (2012); M31 bulge: L_X/M , Revnivtsev et al. (2008), others Brown et al. (2006); M32: age, Monachesi et al. (2012), [Fe/H], Coelho, Mendes de Oliveira & Cid Fernandes (2009), L_X/M , Revnivtsev et al. (2007); NGC 3379; age, Idiart, Silk & de Freitas Pacheco (2007), L_X/M , Revnivtsev et al. (2008).

mass density of the analysed parts of M32 using its de Vaucouleurs profile (Mazure & Capelato 2002). It is important to recognize that most binaries have been processed in the slightly higher density environments of the young clusters in which most stars are born (e.g. Parker et al. 2009), but we use their current densities for this exercise. The parameters we use in our calculations, and their references, are summarized in Table 1. Galaxies often have complex star formation histories; we plot average ages of the bulk of the star formation for our galaxies, using the references in Table 1.

We take measurements of the 0.5–2.0 keV X-ray luminosity per unit mass for old stars (ABs and CVs, with LMXBs and young stellar objects excluded) in our local Galactic disc by averaging two independent measurements; Warwick (2014), who use the *XMM-Newton* slew survey, and Sazonov et al. (2006), who use the *ROSAT* All-Sky Survey and *RXTE* Slew Survey (updated by Revnivtsev et al. 2007). Both estimates partly rely on 2–10 keV measurements, and thus there is some uncertainty in the extrapolation to the 0.5–2.0 keV band. We calculate the 0.5–2.0 keV X-ray emissivity, using Warwick’s 2–10 keV estimates and Warwick’s assumed spectral shapes, as $1.2 \pm 0.3 \times 10^{28} \text{ ergs s}^{-1} M_\odot^{-1}$. Revnivtsev et al. (2007) excluded young stars from Sazonov’s work to find $9 \pm 3 \times 10^{27} \text{ ergs s}^{-1} M_\odot^{-1}$. Thus we choose $1.05 \pm 0.3 \times 10^{28} \text{ ergs s}^{-1} M_\odot^{-1}$ for old stars in the local Galactic disc. For the Galactic field, the binary fraction (including multiples) is taken from Raghavan et al. (2010).

For NGC 3379, Revnivtsev et al. (2008) find $8.2 \pm 2.6 \times 10^{27} \text{ ergs s}^{-1} M_\odot^{-1}$. Since then, Trinchieri et al. (2008) have identified a portion of this emission as being produced by hot gas. However, the inferred diffuse gas component only produces $L_X(0.5–2.0) = 4 \times 10^{37} \text{ ergs s}^{-1}$, or 13 per cent of the total diffuse emission in the 0.5–2.0 keV band. The diffuse X-ray emission from NGC 3379 also includes unresolved LMXBs with $L_X > 10^{36} \text{ ergs s}^{-1}$, as the deep *Chandra* observations do not resolve all sources at this L_X . To remove these, we extrapolate the

$dN/d\ln L$ of NGC 3379 in Kim et al. (2009)’s Fig. 6, and find a total $L_X(0.3–8 \text{ keV}) = 2.1_{-0.6}^{+0.8} \times 10^{38} \text{ ergs s}^{-1}$ from unresolved LMXBs. The errors are derived from assuming either that all LMXBs below $6 \times 10^{36} \text{ ergs s}^{-1}$, or all LMXBs below $3 \times 10^{36} \text{ ergs s}^{-1}$, are unresolved. Assuming a power-law index of 1.7 (Brassington et al. 2010), this gives $L_X(0.5–2.0) = 7.5_{-2.1}^{+2.9} \times 10^{37} \text{ ergs s}^{-1}$, or a further reduction of 24 per cent compared to Revnivtsev’s result, giving $5.2 \pm 1.6 \times 10^{27} \text{ ergs s}^{-1} M_\odot^{-1}$.

We omit the Sculptor dwarf spheroid from our calculations, as discussed in Section 3.3, as we are not certain that any of the X-ray sources identified by Maccarone et al. (2005) are actually associated with this galaxy. Studies of other dwarf galaxies (e.g. Draco, Sonbas et al. 2016) have also failed to confidently identify X-ray sources (except for one symbiotic star; Saeedi, Sasaki & Ducci 2018). We consider the state of the literature on X-ray binaries in dwarf spheroid galaxies to be inadequate to constrain their X-ray emissivity yet.

2.2 Open clusters

We consider five old (>2 Gyr) open clusters, for which deep X-ray observations have been published, and for which estimates of mass and cluster structure exist. Generally we use a 2 keV thermal plasma (MEKAL in XSPEC; Liedahl, Osterheld & Goldstein 1995) to convert reported X-ray luminosities to 0.5–2 keV, as typically assumed for conversions in the open cluster studies mentioned below. We calculate L_X both from the reported point sources of members, and by extracting a spectrum from within the full half-mass radius. We use these two measurements to identify the plausible range of L_X , with the identified members providing a lower limit. We estimate central densities for the open clusters using a simple Plummer model, $\rho(r_0) = \frac{3M_{Pl}}{4\pi R_{Pl}^3}$, where M_{Pl} is the total mass and R_{Pl} is the half-mass radius (e.g. Chumak et al. 2010).

ROSAT observations of M67 and NGC 188 revealed numerous X-ray sources (Belloni et al. 1998). A *Chandra* observation of M67 (van den Berg et al. 2004) allowed clear identification of counterparts (within the *Chandra* field), which combined with proper motion information identified which X-ray sources are members; summing the 0.5–2 keV luminosities of the members gives a total of 3.6×10^{31} erg s $^{-1}$. Alternatively, we extract a spectrum from the 10.5 arcmin half-mass radius (Fan et al. 1996) of M67 from *XMM-Newton* ObsID 0109461001 (using MOS2 and pn data) and fit it simultaneously with a local background spectrum, finding $L_X = 5.9 \pm 0.5 \times 10^{31}$ erg s $^{-1}$. M67’s binary fraction and total mass are taken from Geller, Latham & Mathieu (2015). We estimate a central density of $32 \text{ M}_\odot \text{ pc}^{-3}$ using 2100 M_\odot and a half-mass radius of 2.5 pc (10.5 arcmin at 820 pc).

A full catalogue of X-ray sources in NGC 188 observed by *Chandra* and *XMM-Newton* is reported by Vats, van den Berg & Wijnands (2018) (Gondoin 2005 gives a partial analysis), giving an estimated 0.5–2 keV L_X for members of $2.45 \pm 0.55 \times 10^{31}$ erg s $^{-1}$. We also extract a spectrum from the half-mass region using the *Chandra* observation described in Vats et al. (2018). We subtract stowed background data covering the same detector region from the half-mass spectrum, and also from a nearby background spectrum, and simultaneously fit the half-mass and background spectra to determine the emission from the half-mass region. We adjust the exposure to match the spectra of the source and stowed spectra in the 9–12 keV energy range, scale the sky background by the BACKSCAL values, and fit the additional source component with an APEC spectrum. This gives us $L_X(0.5–2) = 3.3_{-2.9}^{+2.6} \times 10^{31}$ erg s $^{-1}$. (The high uncertainty is largely due to the small area imaged by *Chandra* outside the half-mass radius.)

Mass estimates for NGC 188 range from $1500 \pm 400 \text{ M}_\odot$ (Chumak et al. 2010) to $2850 \pm 120 \text{ M}_\odot$ (Geller, Hurley & Mathieu 2013); we use the estimate of 2300 ± 460 from Geller et al. (2008) as a median that agrees with both. We can estimate a core density of $9 \pm 2 \text{ M}_\odot \text{ pc}^{-3}$ from the Plummer model of Chumak et al. (2010), using their half-mass radius of 4 pc and our mass estimate above. Geller & Mathieu (2012) estimated NGC 188’s binary fraction, covering about 13 core radii from the cluster centre.

NGC 6791 has been studied in detail using *Chandra* by van den Berg et al. (2013), who identify three to four CVs, and twenty likely or candidate active binaries (including ‘red stragglers’ or ‘sub-subgiants’). From van den Berg et al. (2013)’s proper motion and X-ray membership identifications, we estimate the 0.5–2 keV luminosity of NGC 6791 is $(1.04 \pm 0.11) \times 10^{32}$ ergs s $^{-1}$. Fitting the *Chandra* spectrum extracted from the half-mass radius (using the double subtraction procedure as above), we measure $L_X(0.5–2) = 1.12 \pm 0.25 \times 10^{32}$ erg s $^{-1}$, which is nicely consistent. Platais et al. (2011) estimate NGC 6791’s mass to be no lower than 5000 M_\odot (van den Berg et al. 2013 propose $6000 \pm 1000 \text{ M}_\odot$). Using a Plummer model with half-mass radius 5.1 pc (Platais et al. 2011), gives a central mass density of $11 \text{ M}_\odot \text{ pc}^{-3}$. Bedin et al. (2008) estimate NGC 6791’s binary fraction (they quote it for the core, but say it is very similar throughout the rest of the cluster.)

For NGC 6819, Gosnell et al. (2012) report an *XMM-Newton* X-ray study. The certain cluster members among Gosnell et al.’s sources are X5, X6, and X9, using the proper motion membership information of Platais et al. (2013), while the membership of the sources X2 and X4 remains uncertain. Given this membership information, we estimate the 0.5–2 keV luminosity as $(4.8 \pm 2.4) \times 10^{31}$ ergs s $^{-1}$. Note that in Section 2.1 we argue that source X1 is not a cluster member. Extracting spectra from the half-mass region of the *XMM-Newton* MOS data gives $L_X(0.5–2) =$

$6.4 \pm 1.1 \times 10^{31}$ erg s $^{-1}$. The binary frequency of NGC 6819 was found to be 22 ± 3 per cent by Milliman et al. (2014). From its mass of 2600 M_\odot (Kalirai et al. 2001) and half-mass radius of 2.25 pc (e.g. Gosnell et al. 2012), we estimate a central density of $54 \text{ M}_\odot \text{ pc}^{-3}$.

Using *Chandra*, Vats & van den Berg (2017) found a total of 151 X-ray sources in Collinder 261, to a limiting luminosity of 4×10^{29} ergs s $^{-1}$ (0.3–7 keV). Thirty-three of these sources are active binaries and ten to eleven are CVs. From Vats & van den Berg (2017)’s X-ray membership identification, the total X-ray luminosity of point source members of Cr 261 can be estimated as $(8.6 \pm 1.0) \times 10^{31}$ ergs s $^{-1}$ (0.5–2 keV). The *Chandra* spectrum from the half-mass radius of Collinder 261, using the double subtraction method, gives a total $L_X(0.5–2) = 1.1 \pm 0.4 \times 10^{32}$ erg s $^{-1}$, in agreement. For Cr 261, we use an estimated age of 6.5 ± 0.5 Gyr and a distance of 2.45 ± 0.25 kpc from Gozzoli et al. (1996). Using a King profile, Vats & van den Berg (2017) report a mass of 5800 – 7200 M_\odot . We estimate the central mass density at $15 \text{ M}_\odot \text{ pc}^{-3}$.

2.3 Globular clusters

For the cluster parameters distance, metallicity, central density, and reddening, we generally use the Harris catalogue¹ of globular cluster parameters (Harris 1996, 2010 edition), as the distances computed there have the advantage of uniformity, for comparisons between clusters. For mass estimates, we use the calculations of Baumgardt & Hilker (2018), which are in general agreement with the mass estimates of Watkins et al. (2015).²

The M/L_V ratios of clusters differ from each other, showing a standard deviation of ∼20 per cent among the M/L_V ratios in Watkins et al. (2015). Thus, we add an error of 20 per cent in quadrature to the errors on L_X/M on each cluster. Following the lead of the literature (e.g. van den Berg et al. 2013), we include only X-ray sources within the half-mass radius of each globular cluster, and thus divide the inferred masses by 2.³

We use two different sets of globular cluster age estimates, both using the *HST-ACS* survey to compare the relative positions of the horizontal branch and main-sequence turnoff; Marín-Franch et al. (2009), and Vandenberg et al. (2013). We assign GC binary fractions to be those measured by Milone et al. (2012) in the annulus between the core and the half-mass radius (wherever possible), as the most representative of the cluster as a whole.

We list in Table 2 globular clusters for which detailed (typically *Chandra*) X-ray studies have been published identifying the X-ray source content, excluding bright LMXBs. Since this group suffers from observational selection effects (known sources were more likely to be observed), we also focus on a set composed of all globular clusters within 6 kpc, and analyse archival X-ray observations where necessary to produce constraints on all of these clusters. We give details on each globular cluster’s particular properties (including which X-ray sources we regard as secure members) in Appendix A. Here we describe our general procedures.

Trager, Djorgovski & King (1993) separate globular clusters by photometric data quality. We exclude those with the poorest data quality, Terzan 1, Terzan 11/12, and NGC 6540/Djorg 3,

¹<http://physwww.physics.mcmaster.ca/harris/mwgc.dat>

²<https://people.smp.uq.edu.au/HolgerBaumgardt/globular/parameter.html>

³An argument can be made against doing so, as binaries tend to sink into the core during clusters’ evolution; not dividing all cluster masses by 2 would only strengthen our key results.

Table 2. Properties of globular clusters.

Cluster	Expos. (ks)	Dist. (kpc)	$\log(\rho_c)$ ($M_\odot \text{ pc}^{-3}$)	Mass (M_\odot)	Binary per cent	# Srcs (Members)	L_X (half) (Members)	$L_{X, \text{max}}$ ($10^{31} \text{ erg s}^{-1}$)	$L_{X, \text{bg?}}$	$L_{X, \text{min}}$	$2L_X/M$ ($10^{27} \text{ erg s}^{-1} M_\odot^{-1}$)	Reference
N104/ 47Tuc	281	4.5	5.15	7.6×10^5	1.8(0.6)	300(105)	295	270	12	246	5.82 ± 1.28	1,2,3
N3201	83	4.9	2.98	1.3×10^5	10.8(1.2)	40(0)	<7.5	13	9	0	$*0.84 \pm 0.84$	4,6
N4372	10	5.8	2.33	2.2×10^5	—	6(0)	<1.8	*12	30	0	0.63 ± 0.63	5,6
N5139/ ω Cen	70	5.2	3.42	3.4×10^6	—	81	71	130	25	57	0.89 ± 0.39	7,8,9
N6121/M4	26	2.2	3.91	9.1×10^4	10.2(1.0)	21(15)	26	19	4	18	3.64 ± 0.98	10,11
N6218/M12	22	4.8	3.50	8.1×10^4	6.4(0.6)	6(2)	14	10	7	10	1.76 ± 0.46	12
N6254/M10	32.6	4.4	3.81	1.9×10^5	4.4(0.6)	11(1)	6.9	13	4	0.73	0.89 ± 0.81	13,6
N6304	5.3	5.9	4.76	1.5×10^5	—	7(6)	145	81	5	71	15.8 ± 6.3	14,15,6
N6352	19.8	5.7	3.44	6.1×10^4	10.6(1.0)	7(0)	35	19	8	0	5.65 ± 5.65	6
N6366	22	3.5	2.66	5.0×10^4	11.4(3.0)	5(2)	<6	1.9	6	1.4	2.30 ± 1.50	16,6
N6397	49	2.3	6.03	8.9×10^4	2.4(0.6)	79(43)	66	44	1.3	41	15.0 ± 4.6	17,18
N6544	12	2.5	5.72	1.2×10^5	—	7(1)	8.6	6.2	1.5	3.0	1.70 ± 0.89	6,19
N6553	5.2	6.0	4.11	3.3×10^5	—	22(1)	77	47	6	34	$*4.48 \pm 1.95$	6,20
N6626/M28	38	5.5	5.13	3.0×10^5	—	30(3)	288	257	5	247	15.7 ± 3.4	21
N6656/M22	16	3.2	3.90	4.1×10^5	4.0(0.6)	15(2)	18	29	7	7.6	$*0.92 \pm 0.57$	22
N6752	29	4.0	5.31	2.3×10^5	0.9(0.6)	19(10)	36	47	3.0	41	$*4.44 \pm 0.94$	23
N6809/M55	34	5.4	2.49	1.9×10^5	8.0(0.6)	17(2)	<6	11.5	16	4	$*0.93 \pm 0.49$	24,25
N6838/M71	52	4.0	3.10	5.3×10^4	22.0(1.6)	29(10)	13	13	2.8	7	7.50 ± 2.70	26,27
IC 1276	S-2.4	5.4	3.05	9.3×10^4	—	—	<8	—	10	0	1.08 ± 1.08	6
Pal 6	4.6	5.9	3.73	1.4×10^5	—	—	<6.8	—	3	0	0.48 ± 0.48	6
Pal 10	11	5.9	3.78	5.5×10^4	—	—	<18	—	2	0	5.48 ± 5.48	6
Terzan 5	35	5.9	6.15	3.9×10^5	—	50 (4)	557	900	1.5	897	25.7 ± 5.1	29,30,31,32
Beyond 6 kpc												
N288	55	8.8	2.05	1.2×10^5	10.8(1.4)	11(0)	7	19	22	0	2.74 ± 2.74	33
N2808	57	9.6	4.93	8.2×10^5	—	16(2)	137	70	3	70	2.29 ± 0.87	34,35
N6093/M80	49	10.0	5.06	2.8×10^5	1.2(0.6)	17(8)	101	110	3	104	6.90 ± 1.39	36,42
N6144	55	8.5	2.58	5.3×10^4	7.8(1.0)	6(0)	42	19	12	0	3.98 ± 3.98	28
N6341/M92	53	8.3	4.57	3.1×10^5	2.0(0.6)	10(2)	30	24	4.6	20	1.65 ± 0.47	37
N6388	X-25	10.0	5.64	1.1×10^6	0.8(0.8)	61(10)	459	310	3	304	5.59 ± 1.59	38
N6440	23	8.4	5.51	3.8×10^5	—	24(5)	541	400	0.9	398	18.7 ± 4.7	39
N6715/M54	30	26.8	4.96	1.6×10^6	—	7(1)	780	250	11	228	6.25 ± 3.65	40
N7099/M30	49	8.0	5.28	1.3×10^5	2.4(0.6)	13(3)	53	56	5.3	45	6.81 ± 1.54	41
E3	20	8.1	1.11	2.8×10^3	63(41)	3(0)	37	2.8	18	0	53.6 ± 53.6	28,6

Notes. Densities and distances from Harris (1996), 2010 update, except for Terzan 5. Masses from Baumgardt & Hilker (2018). Luminosities are given in the 0.5–2 keV range. ‘Exposure’ column indicates *Chandra* exposure times, except that X indicates *XMM*, S indicates *Swift*. Upper limits on $L_{X, \text{max}}$ indicate that X-ray flux within the half-mass radius is not yet detected. Estimates for the expected ‘ L_X ’ due to X-ray background are provided under $L_{X, \text{bg?}}$, for comparison. Zeroes for $L_{X, \text{min}}$ indicate that no X-ray sources can be confidently identified with the cluster. We quote $2L_X/M$, since we only measure L_X of sources within the half-mass radius. References: (1) Grindlay et al. (2001), (2) Edmonds et al. (2003), (3) Heinke et al. (2005), (4) Webb, Wheatley & Barret (2006), (5) Servillat, Webb & Barret (2008a), (6) this work, (7) Gendre, Barret & Webb (2003), (8) Haggard et al. (2009), (9) Cool et al. (2013), (10) Bassa et al. (2004), (11) Bassa et al. (2005), (12) Lu et al. (2009), (13) Shishkovsky et al. (2018), (14) Guillot et al. (2009a), (15) Guillot et al. (2009b), (16) Bassa et al. (2008), (17) Bogdanov et al. (2010), (18) Cohn et al. (2010), (19) Cohen et al. (2014), (20) Guillot, Rutledge & Brown (2011), (21) Becker et al. (2003), (22) Webb & Servillat (2013), (23) Pooley et al. (2002a), (24) Kaluzny et al. (2005), (25) Bassa et al. (2008), (26) Elsner et al. (2008), (27) Huang et al. (2010), (28) Lan et al. (2010), (29) Valenti, Ferraro & Origlia (2007), (30) Heinke et al. (2006a), (31) Lanzoni et al. (2010), (32) Prager et al. (2017), (33) Kong et al. (2006), (34) Servillat et al. (2008a), (35) Servillat et al. (2008b), (36) Heinke et al. (2003b), (37) Lu et al. (2011), (38) Nucita et al. (2008), (39) Pooley et al. (2002b), (40) Ramsay & Wu (2006), (41) Lugger et al. (2007), (42) Dieball et al. (2010).

along with recently discovered highly obscured clusters such as GLIMPSE-C01 (Kobulnicky & et al. 2005), as for these clusters we cannot reliably determine basic globular cluster parameters such as distance, total stellar mass, and central density. We do include Terzan 5, since its parameters have now been well-determined through infrared and radio pulsar timing studies (Lanzoni et al. 2010; Prager et al. 2017).

Estimating the X-ray emission from actual cluster members is complicated. The most difficult questions are the X-ray emission from non-members, and unresolved X-ray emission. Due to the relatively flat luminosity functions of rich globular clusters (Pooley et al. 2002b), most of the X-ray flux comes from the most luminous sources. *Chandra* and *XMM* exposure times for these clusters vary significantly, but the effect on the total flux normalization

of unresolved sources is typically small for richer clusters. Sources below the detection limits of M28 and M80 ($L_X = 4 \times 10^{30}$ and $L_X = 6 \times 10^{30} \text{ ergs s}^{-1}$) were constrained to produce less than 15 per cent and 5 per cent of the 0.5–2 keV X-ray flux in these clusters, respectively (Becker et al. 2003; Heinke et al. 2003b). Eger, Domainko & Clapson (2010) and Wu et al. (2014) identify likely diffuse emission from the outskirts of Terzan 5 and 47 Tuc, but the flux is <10 per cent of the total from these clusters, and is not attributed to the kind of point sources we study, so we do not include it. Hui, Cheng & Taam (2009) do not find evidence for diffuse X-ray emission in *Chandra* observations of the globular clusters M5, M13, M3, M71, M53, and M4. On the other hand, Bassa et al. (2004) find roughly equal L_X from M4’s core below $L_X(0.5\text{--}2.5) = 6 \times 10^{30} \text{ ergs s}^{-1}$, versus sources from 6×10^{30} up

to $= 6 \times 10^{31} \text{ erg s}^{-1}$, indicating that unresolved emission can produce a significant contribution in the analysis of X-ray faint clusters.

Unresolved, diffuse emission can be difficult to clearly associate with a cluster, while point sources can be linked to particular stars and their membership in the cluster identified. We illustrate the issue with diffuse sources using the case of NGC 6366 (Section 3.2), for which the X-ray emission is dominated by a background galaxy cluster. We approach this problem by calculating X-ray emission from each cluster by both methods – identifying emission from individual sources (and measuring their membership), and using the X-ray emission enclosed within the entire half-mass radius. In most cases, we use estimates for X-ray emission within the half-mass radius from Cheng et al. (2018), and convert them to 0.5–2 keV using either the power-law photon index best fit of Cheng et al. (2018), or a photon index of 2. For clusters not studied by Cheng et al. (2018), we perform this analysis ourselves. When the two estimates (from adding up point sources, or extracting the full flux within the half-mass radius) disagree, we encompass both estimates within our error bars. When we have only upper limits, we impose a minimum $\log L_X/M$ of 25.5 (enabling symmetric errors in the log, necessary for our Monte Carlo fitting).

We identify the maximum L_X for each cluster from all sources within the half-mass radius (column 9 of Table 2). We also compute estimates of the resolved extragalactic X-ray background flux for the half-mass radius of each globular cluster. For typical *Chandra* observations, the resolved soft-band source flux varies from $1.4 \times 10^{-15} \text{ ergs cm}^{-2} \text{ s}^{-1} \text{ arcmin}^{-2}$ for a 20 ks exposure, which reaches (e.g. Lu et al. 2009) a limiting 0.5–2 keV flux of $10^{-15} \text{ ergs cm}^{-2} \text{ s}^{-1}$ (Mushotzky et al. 2000; Giacconi et al. 2001), to $1.8 \times 10^{-15} \text{ ergs cm}^{-2} \text{ s}^{-1} \text{ arcmin}^{-2}$ for a 1–2 Ms exposure resolving sources to $5.5 \times 10^{-17} \text{ ergs cm}^{-2} \text{ s}^{-1}$ (Hickox & Markevitch 2006, table 5).

We compute an expected background flux using $1.7 \times 10^{-15} \text{ ergs cm}^{-2} \text{ s}^{-1} \text{ arcmin}^{-2}$ for each cluster, reported in column 10 of Table 2. The actual background flux is stochastic, depending on what bright AGN happen to lie in this direction. For globular clusters which lie on the Galactic plane, the foreground X-ray source flux can often be higher than that from background sources, and is often not easy to calculate. If the X-ray sources within the half-mass radius are clearly highly concentrated (e.g. most of the flux is within the core), and the maximal L_X is much larger (>3 times) than the expected background flux, then we subtract twice the expected background flux to estimate the minimum L_X , in column 11 (used for NGC 104, NGC 6397, NGC 6544, NGC 6626, NGC 6656, NGC 6752, Terzan 5, NGC 2808, NGC 6093, NGC 6341, NGC 6388, NGC 6440, NGC 6715, NGC 7099). If the X-ray source distribution is not so clearly concentrated, and/or the expected background is of the same order as the observed L_X , then we make reference to identifications (typically optical) of secure cluster members in the literature to determine a minimal X-ray luminosity produced by secure cluster members (column 11 of Table 2). We identify which members we take as secure in Section 2.3.1.

For some nearby clusters, some or all archival *Chandra* observations had not been published (or had only been partly published) when we undertook our analysis; for these clusters (NGC 3201, NGC 4372, NGC 6254/M10, NGC 6304, NGC 6352, NGC 6553, M28/NGC 6626, NGC 6544, Palomar 6, Palomar 10) we analysed the archival data within the half-mass radius. In these cases, we convert the measured cluster $E(B - V)$ to N_H (using Güver & Öznel 2009), and use a power law of photon index 2 to convert the observed 0.5–2 keV counts to flux with the CXC's PIMMS

utility,⁴ accounting for the cycle the data were taken. No *Chandra* or *XMM-Newton* data of IC 1276 has been taken yet; we calculate limits from analysing an archival *Swift* observation. The point of analysing all clusters within 6 kpc is to have a (nearly) complete, distance-limited sample, which we use to investigate the behaviour of L_X/M with central density. Using the observed X-ray fluxes, and minimal X-ray fluxes from known members, for each cluster, we calculate the minimum and maximum L_X values for each cluster in this distance-limited sample. We group these clusters into five ranges in cluster central density (with 4–5 clusters in each group), and calculate the maximal possible ranges in L_X/M for each group (taking the maximum L_X for each cluster, and the minimum L_X , for the extrema), and plot these ranges as magenta rectangles in Fig. 1. A significant trend of increasing L_X/M among globular clusters can be seen at high densities ($>10^4 M_\odot \text{ pc}^{-3}$).

3 THREE INTRIGUING CLAIMS

The key to our analysis is the careful collation of data on a variety of stellar populations. Recent work has added significantly to our understanding of X-ray emissivity in old open clusters (Gosnell et al. 2012; van den Berg et al. 2013; Vats & van den Berg 2017; Vats et al. 2018) and dwarf ellipticals (Ge et al. 2015). To understand the nature of X-ray sources projected on to low-density populations, we feel it is crucial to undertake careful investigation of each source. In Section 5 below, we discuss how a different curation of data have led Cheng et al. (2018) to significantly different conclusions than ours. In this section, we investigate three intriguing claims in the literature, about X-ray sources in (the direction of) the low-density populations of the open cluster NGC 6819, the sparse globular cluster NGC 6366, and the Sculptor dwarf galaxy.

3.1 A neutron star in the open cluster NGC 6819?

The identification of a candidate quiescent neutron star LMXB in the low-density, old, open cluster NGC 6819 by Gosnell et al. (2012) was quite unexpected. X-ray binaries may be formed either primordially or dynamically, but neither method seems plausible here. NGC 6819 is such a low-mass cluster ($2600 M_\odot$; Kalirai et al. 2001) that the chance of finding a primordial NS binary is extremely small. We can roughly estimate this chance, from the following numbers; ~ 200 quiescent LMXBs in Galactic globular clusters (Heinke et al. 2003a; Pooley et al. 2003; Heinke, Grindlay & Edmonds 2005), versus ~ 20 known transient or persistent NS LMXBs in globular clusters (e.g. Bahramian et al. 2014), gives ~ 10 times more quiescent than active NS LMXBs in globular clusters. If this can be extrapolated to the Galaxy, then the ~ 200 known transient or persistent LMXBs (e.g. Liu, van Paradijs & van den Heuvel 2007) imply ~ 2000 quiescent LMXBs in the Galaxy. Kiel & Hurley (2006) indeed estimate 1900 LMXBs in the Galaxy, with other population syntheses predicting 10^3 to 10^5 LMXBs (Pfahl, Rappaport & Podsiadlowski 2003; Jonker et al. 2011). Values of 10^3 – 10^4 LMXBs were favoured by Britt et al. (2013) from analysis of the *Chandra* Galactic Bulge Survey. For a Galactic stellar mass of $\sim 5 \times 10^{10} M_\odot$ (Cox 2000), the full plausible range (10^3 to 10^5 Galactic LMXBs) predicts a probability of 5×10^{-5} to 5×10^{-3} of finding a primordial quiescent NS LMXB in a cluster of $2600 M_\odot$, consistent (on the upper end) with Gosnell et al.'s estimate, made via a very different method. We speculate

⁴<http://asc.harvard.edu/toolkit/pimms.jsp>

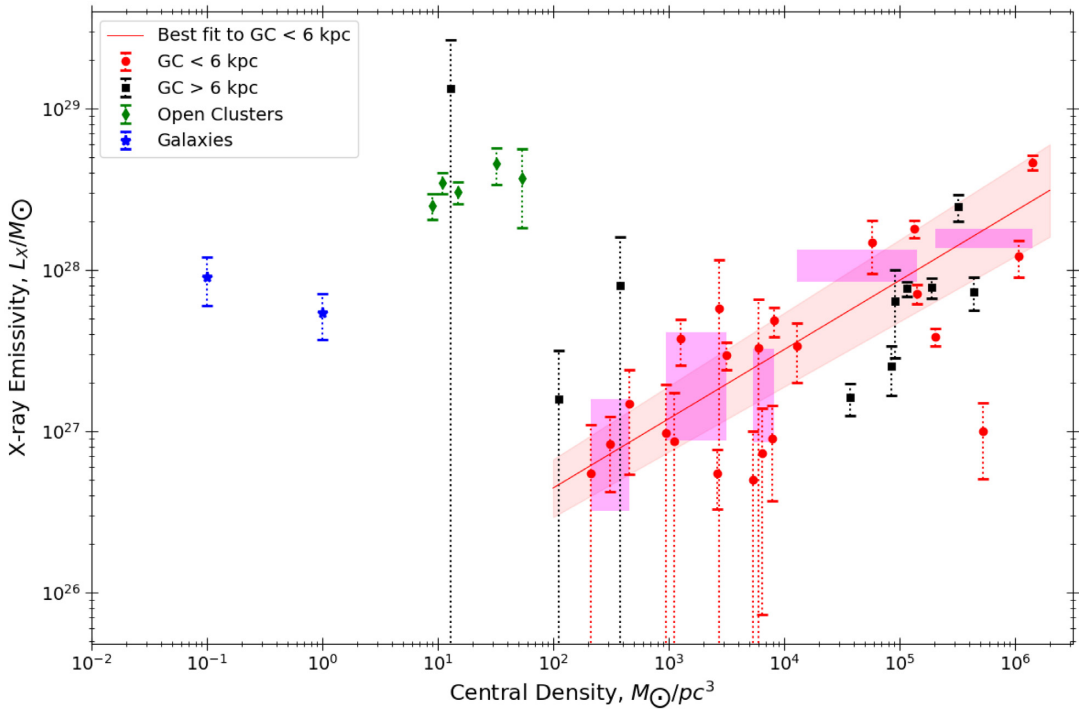


Figure 1. X-ray luminosity (0.5–2 keV) per unit mass for a variety of old systems at various densities, excluding bright low-mass X-ray binaries. Filled circles represent individual populations (red for the GCs within 6 kpc, black for farther GCs), with dotted lines indicating error bars when the membership of X-ray sources is unclear, or X-ray observations provide only an upper limit on the X-ray source content. Magenta rectangles average the GC L_X/M ratios for each of five density ranges for the complete sample of GCs within 6 kpc, including the uncertainties of each cluster. See the text for details.

that, if this open cluster were initially more massive, the probability of hosting an NS LMXB would increase accordingly. However, the hosting probability should also be reduced by the retention fraction of NSs, which should be quite small for a low-mass cluster (e.g. Pfahl et al. 2002).

The low core density of NGC 6819 suggests that strong dynamical effects are unlikely. We use the corrected stellar number counts, down to $V = 21.5$, of Kalirai et al. (2001) to estimate that 20 per cent of its stars are projected within the core. We then estimate the core density of NGC 6819 using this estimate, Kalirai et al.’s estimated total cluster mass of $2600 M_\odot$, NGC 6819’s core radius r_c of 1.64 pc (adjusting Kalirai’s 1.75 pc for the closer 2.34 kpc distance of Basu et al. 2011, as used by Gosnell et al. 2012), giving a rough stellar density ρ of $28 M_\odot \text{ pc}^{-3}$ (assuming an average stellar mass of $1 M_\odot$). Using the simplified prescription for stellar interaction of $\Gamma = \rho^{1.5}/r_c^2$ (Verbunt & Hut 1987), we find that NGC 6819 has a stellar interaction rate of only 2×10^{-7} as large as that of 47 Tuc. (Using a Plummer model as in Section 2, we get a slightly larger density of $54 M_\odot \text{ pc}^{-3}$, and rate 5×10^{-7} that of 47 Tuc.) As 47 Tuc has five known quiescent NS LMXBs (Heinke et al. 2005), this would suggest a probability of $\sim 10^{-6}$ of a dynamically formed NS LMXB existing in NGC 6819. As for the primordial origin pathway, the history of the open cluster could affect this rate (e.g. if it were much denser at early times), but N -body simulations of open clusters (e.g. Hurley et al. 2005) do not suggest that densities comparable to globular clusters are reached. Within this paradigm, it seems that new dynamical pathways to forming LMXBs would be needed (e.g. interactions with triple stars; Leigh & Geller 2013).

In contrast to Gosnell et al.’s conclusions, therefore, we find that any NS LMXB in NGC 6819 would be more likely to be primordial

in origin, though the probability of finding one would be quite small.

This motivates us to check whether the identification of X1 as a quiescent NS LMXB is correct. We first review the arguments of Gosnell et al. (2012). Gosnell et al. (2012) analysed an *XMM-Newton* observation of the moderately old (2–2.4 Gyr; Basu et al. 2011) open cluster NGC 6819. Their analysis of the X-ray spectra and multiwavelength counterparts of the brightest X-ray source projected within the cluster half-mass radius, X1, indicated that it was a quiescent LMXB containing a neutron star. The principal arguments in favour of this classification were: (1) the X-ray spectrum was inconsistent with single-temperature plasma spectra typical of coronally active binaries or cataclysmic variables, but consistent with a quiescent LMXB spectrum; (2) the X-ray position was compatible with a very blue ultraviolet source (in *XMM-Newton* Optical Monitor UVW1 and UVM2 filters), argued to be associated; (3) the ultraviolet position was incompatible with the position of a nearby bright ($V = 16.4$) optical source, identified as a foreground star.

Next, we consider the X-ray spectral information. Fig. 9 of Gosnell et al. (2012) does not appear to show a good fit of the NS atmosphere model to the spectrum from *XMM-Newton*’s pn camera. We downloaded the relevant *XMM-Newton* observation (ObsID 0553510201) and, using SAS 13.5.0, extracted spectra of X1 from the pn, MOS1, and MOS2 cameras, from 15 arcsec radius regions, and nearby background spectra. We constructed response matrices and effective area functions, and grouped each spectrum to 15 counts bin^{-1} . We ignored data below 0.2 keV, and used the *tbabs* interstellar absorption model, with abundances from Wilms et al. (2001).

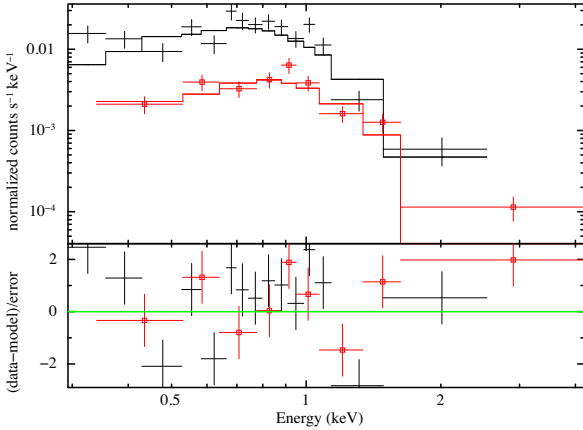


Figure 2. Spectral fit of NGC 6819 X1 to an NS atmosphere, with N_{H} free. Combined MOS data and model in red (with squares), pn data and model in black (data rebinned for plotting purposes). Note the correlated residuals (lower panel), especially to the pn data, below 2 keV.

We begin by trying to fit (using XSPEC⁵) an absorbed NS atmosphere (NSATMOS, of Heinke et al. 2006a), using a 10 km radius, $1.4 M_{\odot}$ mass, 2.34 kpc distance, and normalization = 1 (indicating emission from the full surface). We find that, in accordance with the appearance of Gosnell et al.’s fig. 9, an NS atmosphere is an exceptionally bad fit to the *XMM-Newton* spectra. If N_{H} is fixed to the cluster value of $8.3 \times 10^{20} \mathrm{cm}^{-2}$, the reduced χ^2 is 4.3; when allowed to be free, N_{H} rises to $2.7 \times 10^{21} \mathrm{cm}^{-2}$, but the reduced χ^2 remains 2.05, with 42 degrees of freedom and a null hypothesis probability of 7×10^{-5} . In Fig. 2 we show this latter spectral fit; note the large residuals near 0.5 keV (as mentioned by Gosnell et al. 2012) and generally below 2 keV.

We tried alternative fits using one or two *mekal* (Liedahl et al. 1995) thermal plasma models, as appropriate for coronally active binaries. As noted by Gosnell et al. (2012), a single *mekal* or APEC model gives a poor fit (reduced χ^2 of 2.4). However, coronally active binaries are typically fit with thermal plasma of at least two temperatures. Dempsey et al. (1997) fit *ROSAT* 0.2–2.5 keV spectra of 35 BY Dra dwarf binaries using two-temperature thermal plasmas. The range of best-fitting temperatures for the two components was 0.13 to 0.31 keV for the low-temperature component, and 1.1 to 2.8 keV for the high-temperature component. We found a reasonable ($\chi^2 = 55.95$ for 39 degrees of freedom, null hypothesis probability of 3.8 per cent) fit to the *XMM-Newton* spectra with a two-temperature model (Fig. 3), using $N_{\mathrm{H}} = 0_0^{+2.9} \times 10^{20} \mathrm{cm}^{-2}$, $kT_1 = 0.34_{-0.06}^{+0.07} \mathrm{keV}$, $kT_2 = 1.2_{-0.2}^{+0.2} \mathrm{keV}$.

The two-temperature thermal plasma fit is much better than the fit to a neutron star atmosphere model. The temperatures of the two components are quite compatible with the *ROSAT* results for BY Dra systems. The emission measures for the two components of X1 in our fit are equal, which is also consistent with the *ROSAT* results on BY Dra systems. The preferred N_{H} is significantly lower than the cluster value, indicating a foreground source for this interpretation. Thus we conclude that the X-ray spectrum favours a BY Dra binary interpretation, rather than a quiescent NS LMXB.

Next, we consider the arguments relating to potential optical and UV counterparts. Gosnell et al. (2012) argued against an association between X1 and the nearest optical source, a star far redder than the cluster main sequence that is 1.56 arcsec from the *XMM-Newton*

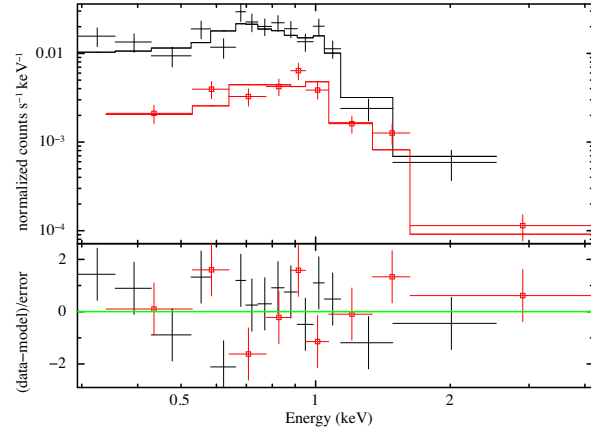


Figure 3. Spectral fit of NGC 6819 X1 to a two-temperature thermal plasma (*mekal* models in XSPEC, $kT = 0.34_{-0.06}^{+0.07}$ and $1.2 \pm 0.2 \mathrm{keV}$), with N_{H} free (it tends to zero). Combined MOS data and model in red (with squares), pn data and model in black (data rebinned for plotting purposes). Note the reduction in residuals compared to Fig. 2.

position for X1 (which has a listed positional error of 1.07 arcsec). This star, known as UCAC4 652-075493 or WOCS 65005 (Hole et al. 2009), is clearly not a member of the cluster (Platais et al. 2013). This star (WOCS 65005) has optical and infrared colours, derived from 2MASS (Skrutskie et al. 2006) and USNO B magnitudes, suggestive of an M0-M1 dwarf. *Gaia*’s Data Release 2 (Gaia Collaboration 2018)⁶ identifies a source with *Gaia* magnitude $G = 15.2$, at J2000 position $\alpha = 19:41:14.14$, $\delta = +40:14:06.58$ (consistent with UCAC4 652-075493’s J2000 position of $\alpha = 19:41:14.13$, $\delta = +40:14:06.74$), at a distance of 155 pc. The observed V magnitude of 16.4 (Gosnell et al. 2012) then gives an absolute V magnitude of 10.45. Consulting the stellar tables of Pecaut & Mamajek (2013), Pecaut, Mamajek & Bubar (2012),⁷ we see that this absolute magnitude matches an M2V star, which predicts $B - V = 1.5$, $J - K_S = 0.834$; the measured values are $B - V = 1.5$ (Gosnell et al. 2012) and $J - K_S = 0.841$ (from the PPMXL catalogue, and thus 2MASS; Skrutskie et al. 2006; Roeser, Demleitner & Schilbach 2010), in nice agreement with the M2V classification.

Instead, Gosnell et al. preferred to associate X1 with a relatively bright UV source detected in the *XMM-Newton* optical monitor *UVW1* and *UVM2* filters, located 1.45 arcsec from the X-ray position of X1. They do not associate the UV and optical sources with each other, because the UV and optical source positions disagree by 0.34 arcsec, a 2σ separation from the quoted errors on each. However, the optical imaging used was performed in 1999 (Kalirai et al. 2001), while the *XMM-Newton* UV imaging was taken in 2008. The proper motion for this star (UCAC4 652-075493) is known to be $38.3 \mathrm{mas \, yr}^{-1}$ in declination (Roeser et al. 2010), or $32.3 \mathrm{mas \, yr}^{-1}$ in declination (Gaia Collaboration 2018), which gives a shift of 0.29–0.34 arcsec in declination over the 9-yr interval. Thus, the optical and UV positions appear consistent with each other. A full astrometric analysis of the UV, optical, and X-ray observations (including more recent *Chandra* imaging) is outside the scope of this paper.

If X1 is located at 155 pc (the distance of the M2V dwarf), its inferred X-ray luminosity is $4.4 \times 10^{29} \mathrm{erg \, s}^{-1}$, quite consistent

⁵<http://xspec.gsfc.nasa.gov>

⁶<https://www.cosmos.esa.int/web/gaia/dr2>

⁷http://www.pas.rochester.edu/~emamajek/EEM_dwarf_UBVIJHK_color_s.Teff.txt

with the range of BY Dra binaries in Dempsey et al. (1997). X1's spectrum is much cooler than the active binaries which are members of NGC 6819 identified by Gosnell et al. (2012), Platais et al. (2013). We attribute this difference in temperature to the tight correlation seen between coronal X-ray luminosity and coronal X-ray temperature (Viana 1983; Güdel 2004). The low N_{H} from our 2-temperature model fit also agrees with the nearby *Gaia* distance.

To determine whether the UV emission observed by Gosnell et al. (2012) is unusual, we consulted the analysis of *GALEX* and *ROSAT* data on active M stars by Stelzer et al. (2013). The near-UV *GALEX* filter covers the wavelength range of 1771 to 2831 Å, comparable to the *XMM OM* filters (UVM2: 2000–2600 Å, UVW1: 2500–3500 Å). The UVW1 flux density from this star is 4.9×10^{-17} ergs cm $^{-2}$ s $^{-1}$ Å $^{-1}$, translating to 5.1×10^{-14} ergs cm $^{-2}$ s $^{-1}$ for the *GALEX* NUV band, or a *GALEX* NUV luminosity of 1.5×10^{29} ergs s $^{-1}$. This luminosity is normal for young active M stars, which typically have soft X-ray luminosities a factor of a few higher than the near-UV, as does our object. Finally, the unusually blue UVM2–UVW1 colour of the X1 counterpart is not unusual for chromospheric, rather than photospheric, emission (Stelzer et al. 2013).

We conclude that all the properties of NGC 6819 X1 are perfectly consistent with a foreground M dwarf binary, and thus treat X1 as a non-member.

3.2 An old nova in the globular cluster NGC 6366?

Bassa et al. (2008) reported X-ray (*Chandra X-ray Observatory*, observed 2002 July 5) and optical (*Very Large Telescope*; *VLT* and *Hubble Space Telescope*; *HST*) observations of the low-density globular cluster NGC 6366. The brightest X-ray source located within the half-mass radius of NGC 6366, CX1, was unusual, containing both a point source (CX1a; $L_X(0.5\text{--}6\text{ keV}) = 1.3 \times 10^{31}$ erg s $^{-1}$) and an extended source (CX1b, $L_X(0.5\text{--}6\text{ keV}) = 1.4 \times 10^{32}$ erg s $^{-1}$), where the quoted L_X values assume NGC 6366's distance of 3.5 kpc (Harris 1996, 2010 update). Both have relatively soft spectra (power law with photon index 3.5 ± 0.6 , and bremsstrahlung with $kT = 2$ keV, respectively; Bassa et al. 2008). Bassa et al. (2008) identified an optical counterpart for CX1a, a $V = 17.75$ star slightly to the red of NGC 6366's giant branch in $B\text{--}R$ and $V\text{--}I$ colour–magnitude diagrams, and with no detectable H α excess. No diffuse optical counterpart to CX1b was seen, in continuum or H α light. Bassa et al. (2008) discussed whether CX1b could be a planetary nebula, supernova remnant, group or cluster of galaxies, or a nova remnant, and argued in favour of a nova remnant. However, this would be a very unusual nova remnant, as CX1b has a much harder X-ray spectrum than the (presumably younger) nova remnant around GK Per (Balman 2005), and the lack of H α emission would also be unusual. Their arguments against a background galaxy cluster were that CX1b's flux and diameter would imply a distance of more than a Gpc (which they thought unlikely), and that their *VLT/FORS2* images showed no obvious galaxies. We investigate the nature of CX1b and CX1a in turn.

3.2.1 Diffuse X-ray source CX1b: A background galaxy cluster

Inspection of the 10 arcsec by 10 arcsec *HST* finding charts in Bassa et al. (2008) reveals the presence of two faint ($V > 21$), extended galaxies, 2 and 4 arcsec to the west of CX1a (see Fig. 4).

One of these galaxies (the western one) is detected in the ACS Cluster Survey catalogue (Anderson et al. 2008), with magnitude

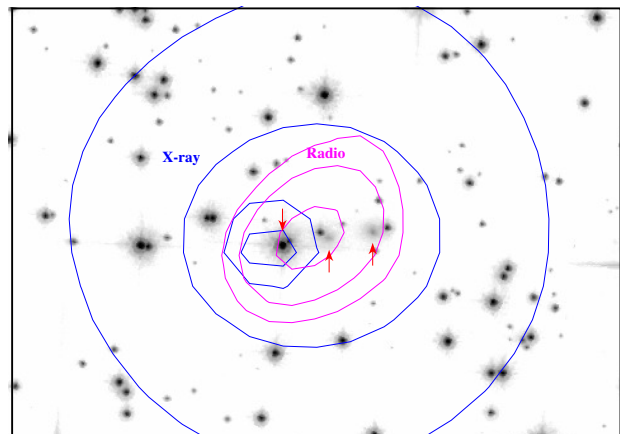


Figure 4. *Hubble Space Telescope* ACS F814W image of part of NGC 6366, with VLA radio (magenta) and Chandra X-ray (blue) contours overlaid. North is up, east to the left, and the black box is 26.0 arcsec by 18.8 arcsec. The point source CX1a is identified by the smallest blue contours, and the bright star within it (indicated by a downward-pointing arrow) is its previously suggested optical counterpart (an alternative counterpart lies just to its NW). The diffuse X-rays of CX1b (two outer blue contours), and the radio emission, are consistent with being centred on the eastern (left) galaxy, of the two galaxies visible within the radio contours (indicated by upward-pointing arrows). This suggests a galaxy cluster as their origin.

$I_{814W} = 21.5$, which for an assumed absolute magnitude of ~ -21 (typical of bright cluster galaxies), and extinction of $A_I \sim 1.04$, implies a luminosity distance of 1.9 Gpc, or a redshift of $z = 0.35$. The other (eastern) galaxy is consistent with Bassa's reported centre of CX1b (see Fig. 4).

The inferred X-ray luminosity of CX1b at this distance would be $L_X(0.5\text{--}6\text{ keV}) = 4 \times 10^{43}$ erg s $^{-1}$, or $\sim 2 \times 10^{43}$ erg s $^{-1}$ in 2–10 keV. This suggests X-ray emission from a (relatively poor) cluster of galaxies, which fits perfectly with its measured ~ 2 keV X-ray spectrum (see e.g. David et al. 1993, their Fig. 5), similar to the cluster of galaxies that Yuasa, Nakazawa & Makishima (2009) identified in the background of the globular cluster 47 Tuc.

We analysed an archival VLA observation of NGC 6366 obtained under observation ID AG627 (PI: B. Gaensler), observed on 2002 September 4. The data were taken at 1.4 GHz in B configuration, with 2 IFs each of 12.5 MHz bandwidth, sampled by 16 channels. A total on-source time of 3.9 h was acquired. We edited, calibrated, and imaged the data in AIPS using standard routines, and an imaging robust value of 0 yields an image rms of 50 microJy beam $^{-1}$ and a synthesized beam of 5.5 arcsec \times 4.7 arcsec.

One source is clearly detected in this image, at 503 ± 49 μJy , centred at J2000 RA = 17:27:42.74, Dec = $-05^\circ 05' 04.8''$. There is no evidence for extension in this image, but the location coincides with that of the eastern galaxy, located at the centre of CX1b.

Fig. 4 shows the radio (magenta) and X-ray (blue) contours, overlaid on an archival *HST* ACS F814W (I) 570 s image, showing that the diffuse X-ray and radio contours are centred on the eastern of the two galaxies. We used the *csmooth* command in CIAO to adaptively smooth (Ebeling, White & Rangarajan 2006) the *Chandra* image.

Comparing the ratio of radio and X-ray fluxes ($\log L_R/L_X = -13.3$, assuming the radio flux is attributed to CX1b) to the tabulations for different source classes in Maccarone et al. (2012), we see that clusters of galaxies typically have $\log L_R/L_X = -13$ to -14 , nicely matching CX1b, while CX1b would be inconsistent

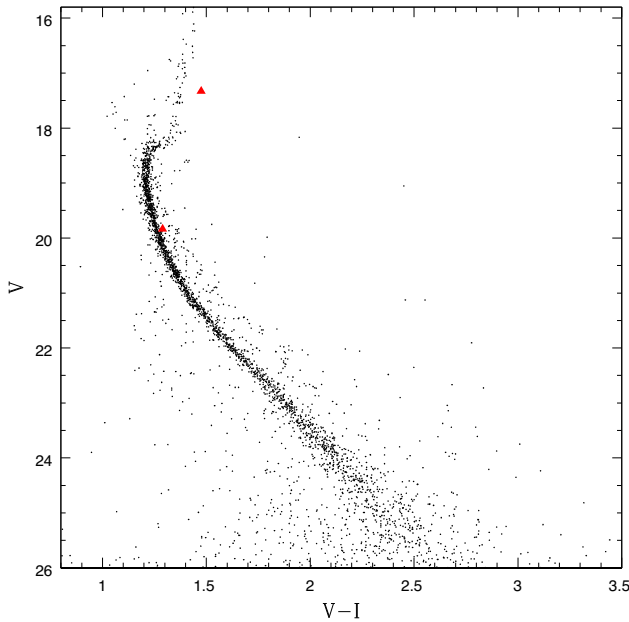


Figure 5. Colour–magnitude diagram from *Hubble Space Telescope* ACS F606W and F814W photometry of NGC 6366, from Anderson et al. (2008). Two red triangles indicate the potential counterparts for CX1a.

with typical values for coronally active stars (-15.5), or cataclysmic variables (<-15). Thus, the X-ray, radio, and optical data of CX1b are all consistent with a background cluster of galaxies, projected on to NGC 6366.

3.2.2 X-ray point source CX1a: A star in the cluster?

The nature of CX1a remains unclear; presumably it is either an AGN associated with the galaxy cluster, or a star in NGC 6366.

Our inspection of the *HST* F606W and F814W imaging of NGC 6366 (Anderson et al. 2008) reveals two stars in the error circle; the bright ($V = 17.33$) star identified by Bassa et al., and a fainter star 0.3 arcsec to the NW, at $V = 19.8$ (see Fig. 4). Fig. 5 uses the Anderson et al. photometry to show a colour–magnitude diagram illustrating the location of the two possible counterparts for CX1a. The fainter star lies on or very near the main sequence, while the brighter star lies to the red of the giant branch, a region with very few stars. The chance of such an unusual star lying within the X-ray error circle is small, while the chance of a normal main-sequence star in the error circle is larger, so we agree with Bassa et al. that the brighter star is the more likely counterpart. However, it is not clear from the CMD position of the bright candidate counterpart that this star is actually a member of the cluster.

To determine its nature, we obtained a longslit optical spectrum of the brighter star in the X-ray error circle (the fainter star will contribute only ~ 10 per cent to the light), using the Gemini Multi-Object Spectrograph (GMOS) on Gemini South, on 2012 September 5 and 10. We took six 900 s exposures with the B600 grating, using a slit width of 2 arcsec (since we used the poor weather queue) and a central wavelength of 520 nm for the first three, 525 nm for the rest (to ensure coverage across detector gaps). The first spectroscopic exposure was taken in bad weather, and the telescope tracking failed; the final three frames have noticeably less noise than the first three.

We reduced the data using the IRAF Gemini package. Two flat-field frames were combined with GSFLAT for each central wave-

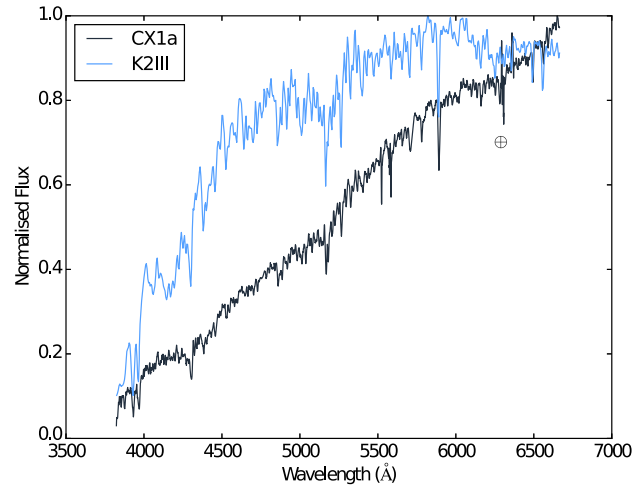


Figure 6. Comparison of our Gemini/GMOS spectrum of CX1a (black) with the normalized library spectrum of a K2 III star from Silva & Cornell (1992) (blue). The location of telluric lines are highlighted by the \oplus symbol.

length. The arc frames were combined for each central wavelength, then bias subtracted, overscan trimmed, and wavelength calibrated using GSWAVELENGTH. The wavelength calibration was refined to yield rms error values of ~ 2 pixels. The science images were bias-subtracted, flat-fielded, overscan trimmed, and wavelength calibrated with the arc frames. A cosmic ray rejection algorithm was applied to each frame during the reduction process. A median frame of the 3 science frames for each central wavelength was created with GEMCOMBINE, taking positional offsets into account, to get the best trace for source extraction. Sky-subtraction was performed on the combined science frames. We extracted the spectrum of the brighter of the two candidate counterparts to CX1a interactively using GSEXTRACT in both images, cross-referencing the slit position with the slit image stamp of NGC 6366 taken at the time of the observations. Additionally, we extracted spectra of the five brightest stars in the slit as reference spectra.

Observations of the standard star (the white dwarf EG21) were reduced in the same manner, except that cosmic ray rejection on the single frame was performed with the L.A. Cosmic algorithm (van Dokkum 2001). The sensitivity function was created using GSSTANDARD. The spectra for each central wavelength were flux calibrated using the sensitivity function, and combined using SCOMBINE. The spectra centred at 525 nm proved to have a higher flux than those at 520 nm, and on inspection showed sharper features. Therefore, we focus on the spectra using the 525 nm central wavelength.

Finally, telluric features were removed by hand using the deblending feature in SPLOT, and the spectra were corrected for velocity dispersion using DISPCOR.

We compared the final spectrum of the CX1a optical counterpart candidate to digital stellar spectra from Silva & Cornell (1992). We do see various spectral lines, which resemble those from a K2-K4 star (Figs 6 and 7). In particular, the relative depths of the Ca II K & H , G band, Mg I, and Na I lines are comparable to mid-K stars.

However, the spectral features are much weaker than in the library spectra. This is especially true of the Balmer drop at 4000 \AA , and the H α and H β absorption lines. This suggests that the (K-class) stellar spectrum may be combined with another, brighter, featureless spectrum, though this hypothesized spectrum would have to be quite red to avoid making the full spectrum bluer.

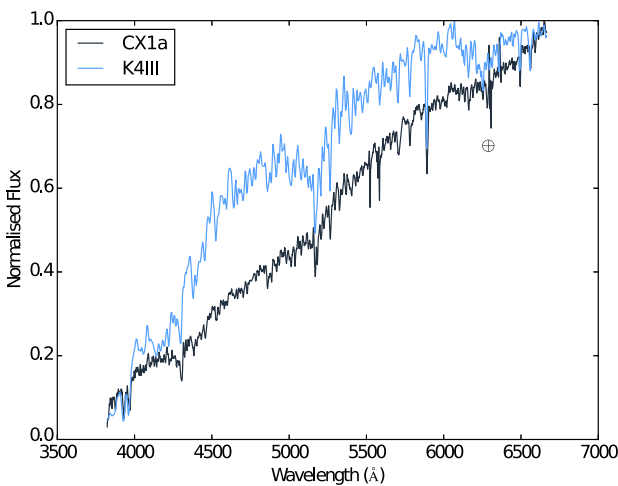


Figure 7. Comparison of our Gemini/GMOS spectrum of CX1a (black) with the normalized library spectrum of a K4 III star from Silva & Cornell (1992) (blue). The location of telluric lines are highlighted by the \oplus symbol.

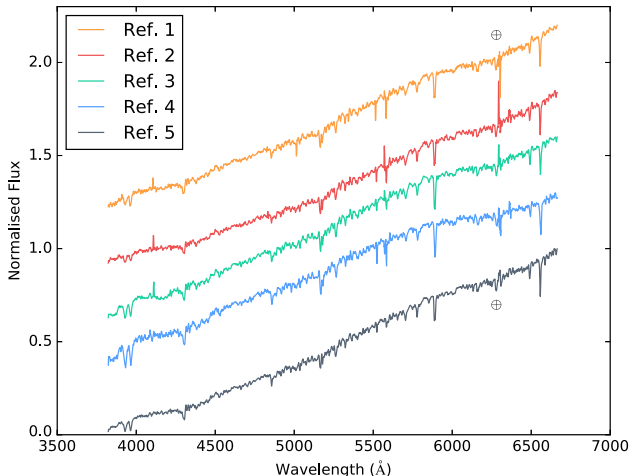


Figure 8. Gemini/GMOS spectra of the five brightest stars in the 2 arcsec slit used to observe CX1a (order as in the legend). The location of telluric lines are highlighted by the \oplus symbol. Apparent emission lines in the spectra are a result of imperfect modelling and subtraction of sky emission lines by the GMOS reduction tools.

A plausible alternative is that the lack of metals in NGC 6366 reduces the strength of the metal lines, compared to the library spectra. Fig. 8 shows the spectra of the five brightest stars also in the slit, all of which exhibit weaker metal features than the library spectra, similar to CX1a.

Another method to test the nature of NGC 6366 CX1a is to compare the relative radial velocity of the optical counterpart with that of other bright objects within the slit. Given NGC 6366's radial velocity with respect to the Earth of -122 km s^{-1} (Rutledge et al. 1997), we should be able to discriminate cluster members from foreground stars, and thus determine if the candidate counterpart to CX1 is a foreground interloper star. Given the density of stars in the cluster, it is likely that most or all bright objects in the slit will be cluster members.

Spectra of the five brightest objects within the slit were extracted to serve as reference stars. The spectra were cross-correlated with templates using the IRAF task FXCOR. This returned the relative

Table 3. Relative radial velocities of reference stars, versus the candidate optical counterpart of CX1a in NGC 6366.

Star	Relative RV (km s^{-1})
CX1a	0 ± 19
Ref. 1	-16 ± 19
Ref. 2	3 ± 19
Ref. 3	-17 ± 24
Ref. 4	-55 ± 39
Ref. 5	5 ± 24

radial velocities uncorrected for dispersion due to position off the centre of the slit.

The 2 arcsec slit width was larger than the seeing of our 525 nm data, introducing shifts in the radial velocities of the reference stars. We attempted to correct for the off-centre positions of the reference objects using the slit image to centroid the location of each star. However, this correction was not fully satisfactory, as relative shifts among the reference stars of $\sim 200 \text{ km s}^{-1}$ remained.

We therefore attempted an alternate wavelength calibration, using telluric and/or interstellar lines in the raw spectra to directly wavelength-calibrate the spectra (using ‘raw’ spectra before telluric-line removal). We were able to identify an O₂ telluric feature near 6282 Å in each spectrum, near a bright sky line whose subtraction leaves prominent residuals. This feature also coincides with a diffuse interstellar band, though for our purposes we do not need to discriminate between the two. We fit the absorption feature (carefully avoiding the residuals from the sky line subtraction) with IRAF’s SPLIT command using a Voigt profile, and estimated uncertainties by selecting slightly larger or smaller regions around the line to include in the fit. We then subtracted the radial velocities of the telluric features from the measured radial velocities of the stellar spectra themselves, giving the values in Table 3. We have not attempted to place these spectra on an absolute basis.

As is clear from the table, the radial velocity of CX1a’s candidate optical counterpart is consistent with the radial velocity of the five reference stars, within the errors of the calibration. Since the typical errors ($\sim 20 \text{ km s}^{-1}$) are much smaller than the radial velocity of the cluster (-122 km s^{-1}), we conclude that this star is certainly a member of NGC 6366.

We also obtained (lower quality) spectra on 2012 June 01 using the 1.6 m telescope at Observatoire Astronomique du Mont-Mégantic (OMM). Three 1800 s exposures were taken through 1.55 to 1.65 air masses during the middle of the night. The long-slit spectrometer consisted of an STA0520 (blue) CCD and a 1200 line mm⁻¹ grating (no filters), yielding a resolving power at 5000 Å of about 5500. Cosmic ray rejection was handled manually and the wavelength calibration was carried out with a CuAr lamp. The fit was better than 0.1 Å (rms) and the calibration was also checked against the strong airglow line [O I] at 5577 Å. The two best spectra were background subtracted, corrected for the quantum efficiency of the detector and the reflectance of the grating, corrected for Rayleigh scattering in the atmosphere, and co-added. Despite a lower S/N ratio than that for the GMOS spectrum shown in Fig. 6, the spectrum is qualitatively similar to a K5-type star. In particular, there are many shallow absorption lines associated with the Fraunhofer group including lines of Mg I, Fe I, and Ca I. Using a Voigt profile for absorption and by correlating several of the cleanest (i.e. minimal line overlap) Fe I, Mg I, and H β lines in the range of 4300 to 5300 Å, we were able to estimate the radial velocity of CX1a as $\simeq -90 \pm 15 \text{ km s}^{-1}$. This result helps strengthen the argument that

CX1a is a member of NGC 6366. The possible deviation from the cluster average of -122 km s^{-1} , if real, is well within the expected range for binary orbital motion.

Finally, we were able to identify this star in *Gaia* Data Release 2 (Gaia Collaboration 2018), where its proper motion is consistent with that of NGC 6366 (Gaia Collaboration 2018; the *Gaia* parallax measurement is not significant yet). Thus, we confirm that all three components of the candidate optical counterpart's velocity are consistent with the motion of NGC 6366.

This exercise does not prove that this star is the true optical counterpart of CX1a, as it remains possible that this star is simply an accidental interloper in the error circle, with the true counterpart being fainter. However, this star is in an unusual position on its CMD, redwards of the giant branch (see Fig. 5). Stars in this position ('red stragglers') are frequently associated with coronally active X-ray sources in open and globular clusters (Belloni et al. 1998; Kaluzny 2003; Cool et al. 2013; Geller et al. 2017). Therefore, we think it very likely that CX1a is associated with this star, a cluster member. The nature of its X-ray emission is not certain, but its X-ray luminosity ($L_X = 1.3 \times 10^{31} \text{ erg s}^{-1}$) and X-ray/optical flux ratio (Bassa et al. 2008) are similar to those of other coronally active stars, including some in similar CMD positions (Geller et al. 2017).

3.3 X-ray binaries in the sculptor dwarf galaxy?

The Sculptor dwarf galaxy is old (>10 Gyr; Monkiewicz et al. 1999; Mapelli et al. 2009) and metal-poor (Mateo 1998), with a total mass of possibly $1.4 \times 10^7 M_\odot$ (Queloz, Dubath & Pasquini 1995), of which roughly $2 \times 10^6 M_\odot$ is stars. A satellite of the Milky Way, it is $86 \pm 5 \text{ kpc}$ away (Pietrzyński et al. 2008).

Maccarone et al. (2005) used 126 ks of Chandra time (in 21 exposures) to identify X-ray sources towards the Sculptor dwarf galaxy. They identified five moderately faint ($L_X \sim 10^{33}-10^{35} \text{ ergs s}^{-1}$) X-ray sources, and three slightly fainter sources, with optical sources, which they argue are on Sculptor's giant and horizontal branches. No bright LMXBs are known in this dwarf galaxy.

Maccarone et al. argued that these systems were quiescent LMXBs, although they are somewhat brighter than typical quiescent LMXBs in our Galaxy. They then inferred that the number of quiescent X-ray binaries per unit mass in Sculptor is $>1/10$ that of the dense globular cluster NGC 6440 (Pooley et al. 2002b; Heinke et al. 2003a). Globular clusters in general contain ~ 100 times more bright LMXBs per unit mass than the Galaxy as a whole (Clark 1975), and NGC 6440 is an unusually dense and LMXB-rich globular cluster (Pooley et al. 2002b), so this might suggest that Sculptor has $\gg 10$ times more LMXBs per unit mass than the Milky Way. Maccarone et al. suggest an alternative explanation, that LMXBs in the Milky Way (and Sculptor) have lower duty cycles (there are more quiescent LMXBs per observed bright LMXB) than LMXBs in globular clusters (the only population where we can measure both, and thus have a rough estimate). In this case, quiescent LMXBs in the Milky Way could be as common (per unit mass) as in Sculptor. However, this explanation conflicts with current observational constraints on the numbers of quiescent LMXBs in the Galaxy (e.g. Britt et al. 2014).

In the 0.5–2 keV band, the lower limit on Sculptor's L_X per unit mass would be $3.5 \times 10^{28} \text{ ergs s}^{-1} M_\odot^{-1}$, if the five XRBs confidently identified by Maccarone et al. (2005) are accepted. This would give Sculptor the highest X-ray luminosity per unit mass of the stellar populations we have studied. This suggests investigation of whether the optical counterparts identified by Maccarone et al. are robust members of Sculptor.

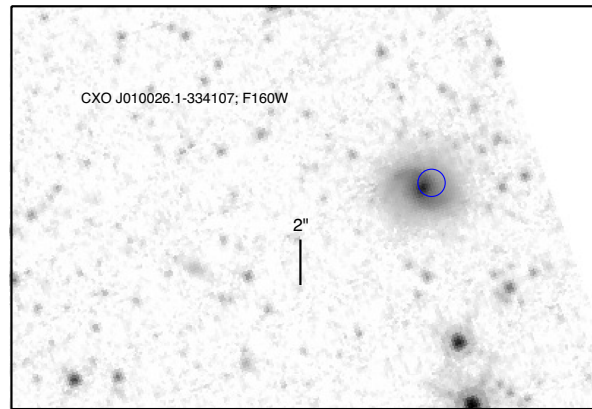


Figure 9. *HST*/WFC3 F160W image of a portion of the Sculptor Galaxy containing Maccarone et al.'s candidate #2 (position indicated by a blue circle of radius 0.6 arcsec). A spiral galaxy is clearly present at the location of source #2.

Maccarone et al. make the following argument: among the nine brightest X-ray sources in their *Chandra* observations of Sculptor, five are within 0.4 arcsec of optical sources with $V < 20.5$ in the catalogue of Schweitzer et al. (1995). The expected number of chance matches of optical sources in this catalogue with the error circles of nine bright X-ray sources is quite low, 0.04. Maccarone et al. argue that these five stars (listed in their table 1) are located on the giant and horizontal branches in Schweitzer et al.'s photometry, and that they have proper motion estimates that indicate probability of at least 96 percent of being members of Sculptor. They also identify a further four matches among fainter X-ray sources (their table 2), one characterized as a background galaxy.

However, we note that Schweitzer et al. do not have sufficient accuracy in their proper motion to measure the Sculptor dwarf's proper motion; they only distinguish between foreground stars with large proper motions, versus objects with small proper motions—such objects could be either Sculptor members, or background objects. Consultation of Schweitzer's CMD reveals that it barely reaches 20.5, the level of the horizontal branch, and that errors are quite large there. Thus, any object near the detection limit with colours bluer than the giant branch could be a potential member of the horizontal branch, or a background galaxy.

We first searched for evidence from *HST* archival images, and then proceeded to investigate archival optical photometry, to assess the plausibility of these objects as cluster members.

We located archival *HST* WFC3 images containing two of the suggested optical counterparts, the 2nd and 5th in table 1 of Maccarone et al. (2005), and downloaded the drizzled, cosmic ray-cleaned images from the STScI archive.⁸ We used the photometry of de Boer et al. (2011), aligned with 2MASS, to correct the astrometry of the *HST* images. For the location of the relevant X-ray sources in Sculptor, which are not provided directly by Maccarone et al. (2005), we use the *Chandra* Source Catalogue, v. 1.1,⁹ to obtain positions and uncertainties.

The location of Maccarone et al.'s X-ray source #2 coincides with a clearly extended object in a WFC3-IR F160W image, identifying X-ray source #2 with a galaxy showing clear spiral structure (Fig. 9).

⁸<http://archive.stsci.edu/hst/search.php>

⁹<http://cxc.cfa.harvard.edu/csc/>

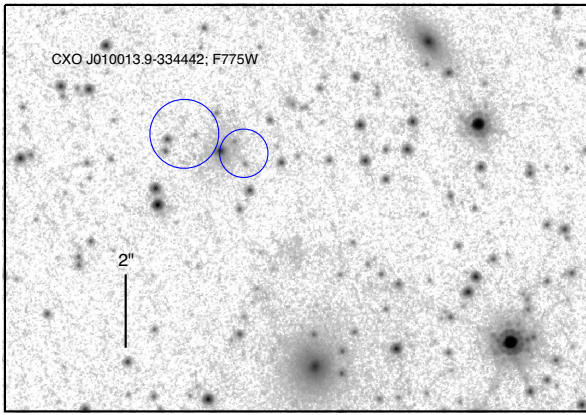


Figure 10. *HST*/WFC3 F775W image of a portion of the Sculptor Galaxy, containing Maccarone et al.’s candidate #5. The position of the X-ray source is indicated by two blue circles, representing two entries in the *Chandra* Source Catalogue v.1.1. A point source surrounded by diffuse emission is clearly present at the intersection of the circles, indicating that source #5 is almost certainly a galaxy.

Arnason et al. (2019) confirms this conclusion from Gemini optical spectroscopy.

Their source #5 appears twice in the *Chandra* Source Catalogue (from different observations), with slightly different positions but similar fluxes ($F_X(0.5\text{--}7 \text{ keV}) = 5 \times 10^{-14} \text{ erg s}^{-1} \text{ cm}^{-2}$), roughly consistent with Maccarone et al.’s reported flux. We plot both positions in Fig. 10, on a WFC3-UVIS F775W image. The two reported positional uncertainties nearly overlap, suggesting that they refer to the same source. Indeed, an optical source (with $I = 22$ in the de Boer catalogue) is visible at the intersection of these circles, suggesting that it is the likely optical counterpart to the X-ray source. Although the optical source initially appears pointlike, close inspection reveals diffuse emission surrounding it which is not present around stars of similar brightness, indicating an AGN nature. (In addition, two other galaxies are clearly visible within 7arcsec). Thus we conclude that sources #2 and #5 are background galaxies. Arnason et al. (2019) identifies an ATCA radio source and a *Spitzer* infrared source with colours typical of AGN, which we find to be $<1\text{arcsec}$ from our suggested optical counterpart. The combined evidence strongly indicates an AGN nature for this X-ray source.

The other suggested counterparts in Maccarone et al. do not have available *HST* imaging. We therefore utilized deeper B , V , and I photometry of the Sculptor dwarf with the MOSAIC-II camera on the CTIO 4 m, presented in de Boer et al. (2011), which has a limiting magnitude of $V = 24.8$.

A search radius of 1 arcsec revealed matches to Maccarone et al. sources #1–8 (from their tables 1 and 2). (Note that Maccarone’s source #9 was identified by them as a background galaxy). However, not all of these had photometry in all filters; #2 lacks an I magnitude, while #5 lacks V and I . We show the locations of those sources with the relevant photometry in Figs 11 and 12.

The photometry of Schweitzer et al. (1995) was not accurate enough to determine if these objects actually lay upon the red giant branch and horizontal branch of the Sculptor dwarf. Using the de Boer photometry, we are able to see that the two faintest sources identified by Maccarone et al. (2005), their source #6 and source #8 ($L_X \sim 3 \times 10^{32}$ and $2 \times 10^{33} \text{ erg s}^{-1}$, respectively), are consistent with the blue end of the horizontal branch, and with the red giant branch, respectively. The remaining objects, sources #1, 2, 3, 4, and 7, do not appear associated with Sculptor’s horizontal branch or red

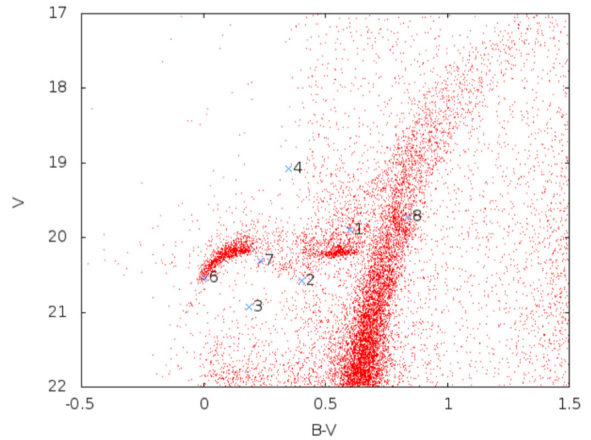


Figure 11. B – V colour–magnitude diagram from the photometry of de Boer et al. (2011) of the Sculptor Dwarf Galaxy, showing the positions of the optical counterparts to Maccarone et al. (2005) X-ray sources.

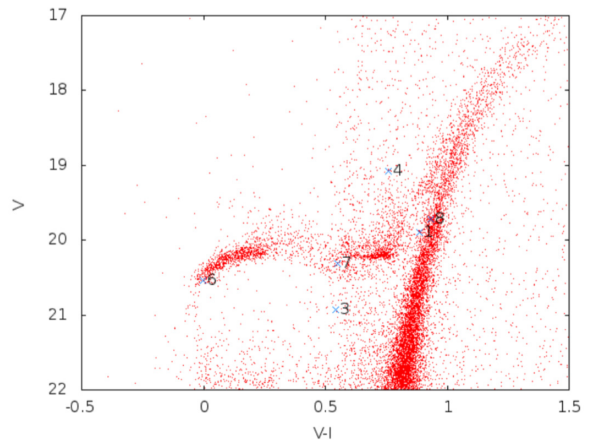


Figure 12. V – I colour–magnitude diagram from the photometry of de Boer et al. (2011) of the Sculptor Dwarf Galaxy, showing the positions of the optical counterparts to Maccarone et al. (2005) X-ray sources.

giant branch. We note that sources #1, 3, 4, and 7 are substantially redder in the V – I CMD than the B – V CMD, when nearby features in the Sculptor dwarf CMD are used for comparison. (Source #2 does not have an I magnitude in this photometry.)

What is the nature of these sources? The unusual colours indicate that either these are not Sculptor members, or that their light is a combination of a (red) Sculptor member plus a hotter component. The estimated luminosities of 6×10^{33} to $6 \times 10^{34} \text{ erg s}^{-1}$ (if members of Sculptor) of these five sources are generally too luminous to be explained as cataclysmic variables, so assuming they are Sculptor members, they would have to be low-mass X-ray binaries with neutron star or black hole accretors (in agreement with the argument of Maccarone et al. 2005). However, the optical light of low-mass X-ray binaries during quiescence is generally dominated by the secondary. For light from an accretion disc to dominate the light of a star at or above the horizontal branch would require a very large mass transfer rate, which would then generate an X-ray luminosity well above $10^{36} \text{ erg s}^{-1}$, which is not seen. We therefore conclude that the optical counterparts to sources #1, 2, 3, 4, and 7 are almost certainly background galaxies (for #2, this agrees with our conclusion from *HST* imaging, above). Arnason et al. (2019) reports Gemini spectra that confirm an AGN nature for

objects #1, 2, 3, and 4, and *Spitzer* infrared photometry indicative of an AGN nature for #7.

The nature of sources #6 and 8 are less clear, as their optical counterpart colours and luminosities are consistent with members of the Sculptor dwarf. The potential optical counterpart to source #6 is almost certainly a star in Sculptor, as its position on the blue horizontal branch in two filter combinations would be extremely unlikely to occur by chance for a background galaxy. Arnason et al. (2019) identify the likely counterpart to #6 in their *Spitzer* infrared and Gemini optical photometry, with colours typical of similar stars (including H α absorption typical of stars of this temperature), and discuss an optical spectrum to the possible counterpart to #8 that shows no emission lines. A background galaxy nature is quite plausible for these two sources, as the Sculptor stars could be chance alignments (the stellar density in this region is such that each 1.5 arcsec error circle should have a roughly 10 per cent chance of capturing a spurious match). Further spectroscopy, high-resolution imaging (to rule out association with extended galaxies, as we found for #2 and 5 above), and/or proper motion studies could clarify their nature.

Since we have no robust identifications of X-ray sources associated with the Sculptor dwarf, we do not attempt to calculate the X-ray emissivity of the Sculptor dwarf galaxy in this work.

4 WHAT INFLUENCES X-RAY EMISSIVITY?

From the data assembled in Sections 2 and 3, we investigate several possible variables that may affect X-ray emissivity.

We explore the dependence of X-ray emissivity on four interesting variables: age, binary fraction, metallicity, and density. We utilize several methods to test the importance of each variable (and combinations of variables), including (1) least-squares regression analysis using a Markov Chain Monte Carlo (MCMC) method and the No-U-Turn Sampler (NUTS) algorithm to handle errors in both variables by sampling from the uncertainty distributions; (2) bootstrapping (random sampling with replacement); and (3) Pearson and Spearman correlation tests.

Stellar interactions are well-known to produce more X-ray binaries in higher density globular clusters (e.g. Verbunt & Hut 1987). We plot central density versus X-ray emissivity in Fig. 1, grouping globular cluster populations at similar central densities together to improve statistics. Among globular cluster populations, we see evidence of a significant increase in X-ray emissivity with central density, which becomes clear above $10^4 M_\odot pc^{-3}$. Below $10^4 M_\odot pc^{-3}$, it is unclear whether there is any trend with central density. We do see that populations outside globular clusters have substantially higher X-ray emissivity than in lower density globular clusters, as first identified by Verbunt et al. (2000), and discussed by several other authors (see the Introduction). Fig. 1 shows that this discrepancy occurs among populations that in some cases have similar central densities.

For several of the low-density systems plotted, we know the major contributor(s) to the X-ray luminosity. In our local region of the Milky Way disc, the old stellar population's X-ray emission is dominated by ABs, though there are numerous unidentified sources in all surveys (Sazonov et al. 2006; Agüeros et al. 2009; Warwick 2014). In M67, the total X-ray luminosity is dominated by short-period (1–10 d) ABs (\sim half the L_X), and by longer period binary stars whose X-ray emission is not well understood (most of the remainder; van den Berg et al. 2004). NGC 6791 hosts four known CVs, which produce a substantial fraction of its X-ray luminosity (Kaluzny et al. 1997; de Marchi et al. 2007; van den Berg et al.

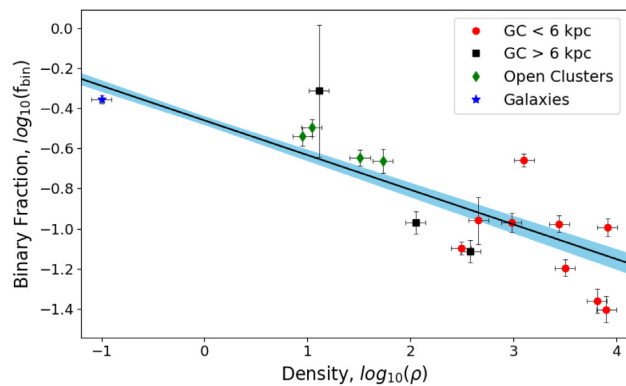


Figure 13. Central density plotted against binary fraction of clusters, for central densities less than $10^4 M_\odot pc^{-3}$. The observational errors were assumed to be $1-\sigma$ error bars for all the properties of the clusters, which are required to be symmetric in our code. NUTS was used to sample the parameter space and obtain best-fitting values along with its error. From that, we generate a $1-\sigma$ MCMC error region of the fit, shaded in blue. We observe a negative correlation between binary fraction and central density.

2013). In order to reduce the X-ray luminosity per unit mass by an order of magnitude in globular clusters compared to other systems, both types of X-ray emitting binaries must be reduced in frequency.

In this work, we concentrate on trying to understand the parameters that affect the X-ray emissivity at central densities below $10^4 M_\odot pc^{-3}$, leaving the analysis of how density-dependent stellar interactions produce X-ray binaries for other works. We consider several possible parameters; age, metallicity, binary fraction, and density of the stellar populations. Binary fraction and density are significantly anticorrelated (see Fig. 13 for a demonstration among our sample), as shown by Milone et al. (2012), though this may be a side effect of the even stronger correlation between binary fraction and total cluster mass. Unfortunately, density, metallicity, and age tend to be strongly correlated (as globular clusters are dense, old, and metal-poor). Our goal is to identify what parameters seem to most strongly influence X-ray emissivity, and to what degree.

4.1 Bayesian analysis

We look for the strongest correlations between X-ray emissivity and combinations of the parameters of age, binary fraction, metallicity, and/or density. We first compare the parameters individually against X-ray emissivity, then try more complicated comparisons of combinations of parameters. We use two methods of performing linear fits: (i) likelihood maximization using the MCMC sampling method and (ii) bootstrapping, a random sampling of the data with replacement. We also assess correlations using two statistical measures: (i) Pearson correlation coefficient (r) and (ii) Spearman's rank-order coefficient (ρ).

MCMC is a sampling method that deals well with ‘nuisance’ parameters or data with poorly determined errors. Some of our clusters only have an upper limit on their luminosities (such as NGC 6352 in Table 2, etc.), and some have predicted background X-ray luminosities that are comparable to the maximum X-ray luminosities, if not higher (such as NGC 3201 in Table 2, etc.). Also, there are several galaxies with large errors in metallicity (NGC 205, 221, and 224), so the most flexible way we found to address these

Table 4. Correlation coefficients (for Pearson, Spearman tests) and appropriate p-values for several comparisons. Each comparison includes either (All), just (GCs), or just (Non-GC) data, as specified. Age tests use (MF) = Marín-Franch et al. (2009) ages, or (V) = VandenBerg et al. (2013) ages for GCs. Column 6 identifies the relevant figure showing each correlation.

Comparison	Pearson Coeff.	Prob.	Spearman Coeff.	Prob.	Figure
f_{bin} versus ρ_c (All)	-0.837	<0.01	-0.816	<0.01	Fig. 13
L_X/M versus:					
ρ_c (All)	0.114	0.49	0.195	0.24	–
ρ_c (GCs)	0.676	<0.01	0.735	<0.01	Fig. 1
ρ_c (Non-GCs)	0.966	<0.01	0.821	0.02	–
Age (V; All)	-0.644	<0.01	-0.677	<0.01	–
Age (V; GCs)	0.016	0.96	0.000	1.000	Fig. 14
Age (Non-GCs)	-0.271	0.39	-0.375	0.23	–
Age (MF; All)	-0.462	0.02	-0.346	0.09	–
Age (MF; GCs)	0.670	0.01	0.735	<0.01	Fig. 15
Fe/H (All)	0.620	<0.01	0.562	<0.01	–
Fe/H (GCs)	0.215	0.41	0.172	0.51	Fig. 16
Fe/H (Non-GCs)	0.314	0.32	0.378	0.23	–
f_{bin} (All)	0.553	0.02	0.461	0.06	–
f_{bin} (GC)	0.464	0.13	0.259	0.42	Fig. 17
f_{bin} (Non-GC)	-0.848	0.07	-0.500	0.39	–

problems in the analysis was to use a Bayesian analysis method, more specifically MCMC as our main sampling fitting method. We use PyMC3¹⁰ from Salvatier, Wiecki & Fonnesbeck (2016) and its implementation of the No U-Turns Sampler (NUTS). Our analysis uses logarithms of the relevant quantities, which are better handled by MCMC routines than variations by many orders of magnitude among the data. Our code requires symmetric error bars (in log space); we find the 1-sigma error range and use this to compute a mid-point (in log space). When we have only an upper limit on L_X/M , we enforce a lower limit of $\log(L_X/M_\odot) = 25.5$.

We use the Gelman–Rubin diagnostic (R) to test for convergence. We sample our models for 5000 steps with 1500 burn-in steps and obtain values of R within 0.0002 of 1.0000, which indicates that the fit procedure is well-behaved.

We also apply a bootstrapping procedure to test the robustness of our MCMC fitting to our sample selection. Bootstrapping attempts to compensate for stochastic variation in the selection of our sample, by performing the same fit repeatedly with different samples. The new samples are constructed by sampling from the original data with replacement until the same number of data points has been reached, but with some data points potentially duplicated, and others omitted. We perform one hundred thousand iterations of such random subsets.

We also calculate both Pearson and Spearman correlation coefficients for the correlation between each variable and X-ray emissivity. The Spearman test is less affected by outliers in the data (as the data is only sorted by rank), while the Pearson test assumes all data have the same errors. Thus, the Spearman test is arguably more appropriate for data sets where some of the data have much larger errors (e.g. see the large errors for E3). The scores for each fit are calculated and tabulated in Table 4.

4.2 Effects of age, metallicity, binary fraction, and density

As discussed above (Sections 1 and 4), there is evidence from previous work, and within our sample, for a correlation of density with X-ray emissivity. Fig. 1 suggests that this effect is clearly visible only at high central densities. We quantify this with our PyMC3 NUTS regression using various subsamples: all objects, all globular clusters, and objects with densities lower or higher than $10^4 M_\odot \text{ pc}^{-3}$.

For the complete sample, we find a very weak correlation between X-ray emissivity per unit mass and stellar density, with a best-fitting slope of -0.04 ± 0.01 and weak Pearson and Spearman coefficients (0.11 and 0.20, p-values 0.49 and 0.24, respectively, Table 4). However, the globular cluster sample alone shows a very strong correlation, with p-value <0.01 of occurring by chance. When dividing the sample into parts with density above and below $10^4 M_\odot \text{ pc}^{-3}$, we find that neither sample shows strong correlations. We suggest that this is due to density having a strong effect on X-ray emissivity only for the higher density population; specifically, that only in high-density globular clusters are substantial numbers of X-ray binaries formed dynamically. Fig. 1 suggests that the threshold for this effect lies around $10^4 M_\odot \text{ pc}^{-3}$.

Next, we test the remaining parameters (age, metallicity, and binary fraction) individually against X-ray emissivity, for stellar populations with central density less than $10^4 M_\odot \text{ pc}^{-3}$. We are particularly interested in the low-density population, since dynamically formed globular cluster populations, produced at high density, may have different dependences on these parameters than populations that are not formed dynamically.

The age of a stellar population is likely to affect its X-ray populations. CV population mass transfer rates are correlated with companion mass, so are likely to decline with age as the masses of available companions decline (e.g. Stehle, Kolb & Ritter 1997; Ivanova et al. 2006). At the same time, X-rays from normal stars strongly decline with age as the stars spin-down (e.g. Randich 1997), but after 1 Gyr the AB X-ray luminosity dominates, and we do not know how this varies with time. (Close ABs spiral together and merge, but wider binary orbits shrink, causing initially wider ABs to produce stronger X-ray emission later).

The measurement of ages of stellar systems is a difficult art, particularly when small differences in ages among old populations are sought. Several recent works have measured the (relative, or absolute) ages of globular clusters; these include Marín-Franch et al. (2009), De Angeli et al. (2005), VandenBerg et al. (2013), Hansen et al. (2013), and O’Malley, Gilligan & Chaboyer (2017). However, there are substantial differences between the relative ages of globular clusters in these works, suggesting that age measurement is not a settled subject. We use the two studies with the largest overlap with our cluster sample, Marín-Franch et al. (2009) and VandenBerg et al. (2013), and compare calculations using either sample. Marín-Franch et al. (2009) give only relative globular cluster ages; we assume an average age of 10.7 Gyr (which matches the age of 47 Tuc, and the average for outer halo globular clusters in general, from Salaris & Weiss 2002) to place these on an absolute scale.

Figs 14 and 15 compare X-ray emissivity versus age estimates for our sample (using the two globular cluster age studies). Galaxies often have complex star formation histories, so we plot the average ages of the bulk of the star formation for our galaxies as referenced in Table 1. For our regression analyses with one parameter, our independent variables are the slope and intercept of a line through the data. Our PyMC3 calculations find that the most likely correlation between age and X-ray emissivity is negative. The slope of the fit

¹⁰<https://docs.pymc.io>

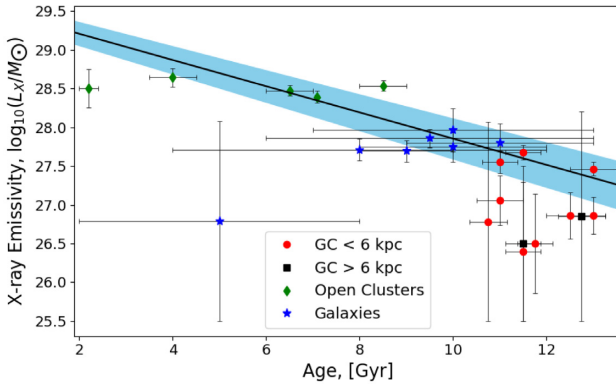


Figure 14. X-ray emissivity versus age (VandenBerg et al. 2013 estimates for globular clusters), using clusters with central luminosity densities less than $10^4 M_\odot \text{ pc}^{-3}$. See Fig. 13 and the text for details.

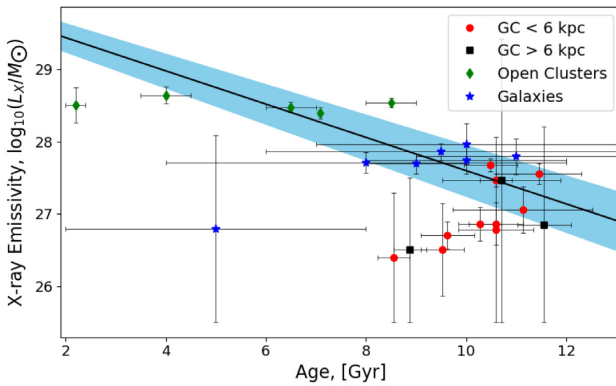


Figure 15. X-ray emissivity versus age (Marín-Franch et al. 2009 estimates for globular clusters), using clusters with central luminosity densities less than $10^4 M_\odot \text{ pc}^{-3}$. See Fig. 13 and the text for details.

using the VandenBerg et al. (2013) ages in Fig. 14 is -0.16 ± 0.02 , while the fit using the Marín-Franch et al. (2009) ages in Fig. 15 is -0.22 ± 0.02 . The error range, including slope and intercept errors, is shaded in blue. We confirm the negative correlations by calculating the Pearson and Spearman coefficients for the correlation of age versus L_x/M , finding coefficients of -0.64 and -0.68 (each have p-values <0.01 of obtaining such a high correlation by chance) using the VandenBerg et al. (2013) ages, and -0.46 and -0.35 (p-values 0.02 and 0.09, respectively) using the Marín-Franch et al. (2009) ages, respectively (Table 4). The correlations appear to be due principally to different populations having different average ages, without apparent correlations between emissivity and age within each population. We suspect these apparent correlations are really due to the other fitted parameters (see below).

Considering only the non-GC populations, the correlation between L_x/M and age is insignificant ($p = 0.39$ and 0.23 for the Pearson and Spearman tests, respectively), and appears to be due to differences between the emissivities and average ages of the galaxy and open cluster populations, which have wide, overlapping age ranges; see Fig. 14. For the GC sample alone, the Marín-Franch and VandenBerg ages give opposite slopes for the L_x/M versus age relation (see Figs 14 and 15); interestingly, the Marín-Franch ages indicate a significant positive correlation ($p = 0.01$) between age and L_x/M (Table 4), the opposite of what we expected. Uncertainties in the age measurements limit the power of this analysis.

Metallicity is known to be a factor affecting the frequency of bright LMXBs in extragalactic globular clusters (e.g. Kundu et al. 2003), and of their descendants, millisecond pulsars (e.g. Hui et al. 2011). A clear effect of metallicity has not been found for faint X-ray binaries so far (e.g. Heinke et al. 2006b), but this could be due to a relatively small number of studied sources. Stehle et al. (1997) model low-metallicity CV evolution, finding slightly higher mass-transfer rates, which would lead to shorter CV lifetimes, while Côté et al. (2018) find larger numbers of accreting WDs in CV-like systems at low metallicity in their models. Thus, there is not yet a clear, accepted prediction for the effects of metallicity on L_x/M for CVs. We note that the mass-to-light ratio may vary with metallicity (as suggested by stellar population models, e.g. McLaughlin & van der Marel 2005, but cf. Watkins et al. 2015 and Strader, Caldwell & Seth 2011 who find the opposite dependence), which may generate an apparent metallicity effect on X-ray emissivity. Baumgardt & Hilker (2018) do not find a correlation of mass-to-light ratio with metallicity, and we use their mass estimates, which suggests that any metallicity effect is not due to mass-to-light ratio variance.

We plot in Fig. 16 X-ray emissivity versus the metallicity of the moderate and low-density globular clusters (central density $< 10^4 M_\odot \text{ pc}^{-3}$). A trend towards higher X-ray emissivity among higher metallicity systems is clear, and the trend may be visible among the globular cluster population as well as the non-GC population. Our PyMC3 calculation finds a slope of 0.69 ± 0.06 for the best fit of metallicity versus L_x/M for all low-density systems, suggesting a much larger effect than age. We find strong evidence of correlation from the Pearson and Spearman tests, with chance probabilities <1 per cent (Table 4). We also computed correlation coefficients for the globular cluster population and non-GC population separately, but did not detect a significant correlation for either population individually. The non-GC systems have significantly higher X-ray emissivity than globular clusters of the same metallicity, suggesting that another variable plays a larger role.

The fraction of cluster members that are binaries is a clearly plausible parameter to explain the X-ray emissivity variations among different populations. All X-ray emitting populations of old stars are produced in binary systems of some kind; ABs, CVs, LMXBs, and MSPs are binaries, or descend from binaries. A significant caveat is that each type of X-ray emitting system may be produced by binaries of different initial orbital period and component masses, and that the distribution of binaries in a population cannot be completely described by a single number, the binary fraction. In particular, X-ray emitting binaries are generally in relatively short orbits ($<< 1 \text{ AU}$), while the differences in binary fraction among different populations may be strongest among longer orbit systems, which are vulnerable to disruption at moderate densities (Hut et al. 1991). However, systems in close orbits will have previously been longer period binaries, with periods reduced by angular momentum loss, or (more strongly) by common envelope evolution.

Fig. 17 shows the correlation between binary fraction and X-ray emissivity among our sample. Unfortunately, relatively few of our populations have measured binary fractions, so we have a significantly smaller sample here than in the other comparisons. Our PyMC3 calculations give a slope of 1.82 ± 0.20 , the largest fitted slope of any parameter. Pearson and Spearman tests indicate significant, or marginally significant, correlations ($p = 0.02$ and 0.06, respectively; Table 4). We also checked for correlations among the subsamples of all globular clusters and all non-globular clusters, but did not find statistically significant ($p < 0.05$) results for either independently (these have the smallest sample sizes among our investigated samples).

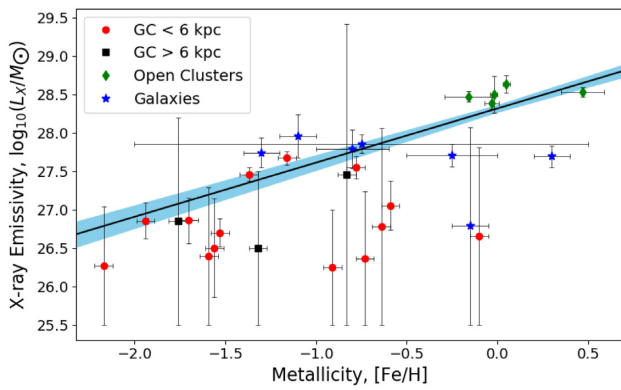


Figure 16. X-ray emissivity plotted versus metallicity, using clusters with central luminosity densities less than $10^4 M_\odot \text{ pc}^{-3}$. See Fig. 13 and the text for details.

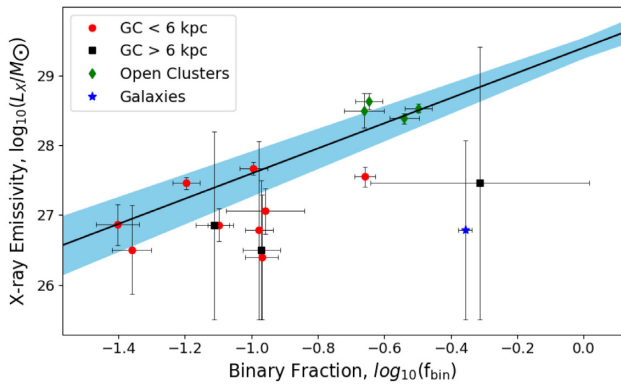


Figure 17. X-ray emissivity plotted against binary fraction, using clusters with central luminosity densities less than $10^4 M_\odot \text{ pc}^{-3}$. See Fig. 13 and the text for details.

Finally, we explore combinations of the promising variables of binary fraction, metallicity, and density. We first performed an analysis including age along with the other parameters, but found that this number of parameters led to a poorly constrained fit. Given the lack of strong evidence for age alone as a parameter, and the uncertainty in relative ages among different methods, we omit age from our principal analyses. We set weights by taking binary fraction to the power α , metallicity to the power β , and density to the power of γ ,

$$\frac{L_X}{M} = (f_{\text{bin}})^\alpha \times (10^{[\text{Fe}/\text{H}]})^\beta \times (\rho)^\gamma \times 10^b. \quad (1)$$

We find it convenient to take logarithms of both sides, so as to perform the fit in linear space allowing easier measurement of the contribution of each variable. This gives

$$\begin{aligned} \log_{10} \left(\frac{L_X}{M} \right) &= \alpha(\log_{10}(f_{\text{bin}})) + \beta([\text{Fe}/\text{H}]) \\ &\quad + \gamma(\log_{10}(\rho)) + b. \end{aligned} \quad (2)$$

We set up the priors in the following way:

$$\alpha, \beta, \gamma \sim \mathcal{N}(0, 5)$$

$$b \sim \mathcal{N}(0, 50)$$

$$\log_{10} \left(\frac{L_X}{M} \right)^* \sim \mathcal{N} \left(\log_{10} \frac{L_X}{M}, \sigma_{\log_{10} L_X/M} \right) \quad (3)$$

Table 5. The best-fitting values and errors (1σ) for the exponent parameters (and intercept) from our PyMC3 fits, fitting density, binary fraction, and metallicity (see Fig. 18). The first column of fits include all our samples, the second include all samples with a density less than $10^4 M_\odot \text{ pc}^{-3}$, the third is all samples with densities above that, while the last column includes only all the globular cluster samples.

MCMC	All ρ	Low ρ	High ρ	GCs
α , on f_{bin}	$1.04^{+0.14}_{-0.15}$	$-0.60^{+0.54}_{-0.49}$	$0.32^{+1.29}_{-1.07}$	$0.63^{+0.15}_{-0.18}$
β , on $[\text{Fe}/\text{H}]$	$0.60^{+0.09}_{-0.09}$	$1.01^{+0.21}_{-0.24}$	$0.10^{+0.16}_{-0.11}$	$0.15^{+0.09}_{-0.07}$
γ , on ρ	$0.39^{+0.06}_{-0.07}$	$0.03^{+0.09}_{-0.08}$	$0.55^{+0.13}_{-0.14}$	$0.49^{+0.06}_{-0.07}$
b, on L_X/M	$28.3^{+0.1}_{-0.1}$	$28.0^{+0.3}_{-0.3}$	$25.6^{+2.8}_{-2.0}$	$26.6^{+0.2}_{-0.2}$
Pearson	0.540	0.754	0.832	0.705
p-value	<0.01	<0.01	0.02	<0.01
Spearman	0.469	0.699	0.571	0.770
p-value	0.02	<0.01	0.18	<0.01

α , β , γ , and b are the exponents on the variables of binary fraction, metallicity, and density, as defined in equation (1). We use wide, uninformative priors to emphasize the data's contribution in the likelihood function. We also define a prior, $\log_{10}(L_X/M)^*$, to describe each individual point in the X-ray emissivity.

The likelihood function is written as

$$\begin{aligned} p(y_i | \mu, \sigma) &= \sqrt{\frac{1}{2\pi\sigma^2}} \exp \left(-\frac{(y_i - \mu)^2}{2\sigma^2} \right) \\ \mathcal{L} &= \prod_{i=1}^N p \left(y_i | \log \left(\frac{L_X}{M} \right), \sigma_{\log \left(\frac{L_X}{M} \right)} \right) \text{priors}, \end{aligned} \quad (4)$$

where μ equals the expected outcome for the X-ray emissivity, which is defined as the model represented by equation (2), and σ is the error of the X-ray emissivity.

Sampling this space using the NUTS algorithm, we generate the parameter distributions as listed in Table 5 for four different groups – all data, all low-density objects ($\rho < 10^4 M_\odot \text{ pc}^{-3}$), all high-density objects, and all globular clusters. We divide the data by density, due to our hypothesis that high-density environments produce X-ray sources through dynamical processes, with different dependencies than the normal methods of producing these sources at low density. We also check the results for the globular cluster subsample specifically.

Fits to the full data set ('All ρ ' in Table 5) found two minima in the MCMC chains. However, one of these fits had large negative coefficients on both binary fraction and density. We opted to impose a prior that the binary fraction coefficient be positive, selecting the more physically plausible solution, which also gave a statistically better fit. This fit gives strong Pearson and Spearman correlation coefficients (0.54 and 0.47; probabilities <0.01 and 0.02), indicating that the fitted parameters are well-correlated with the X-ray emissivity, although there remains significant scatter (see Fig. 18). We find significantly non-zero exponents for binary fraction, metallicity, and density, indicating that all three variables contribute to the variance in X-ray luminosity. The highest exponent ($1.04^{+0.14}_{-0.15}$) is on binary fraction, suggesting that this is the most important parameter. However, the substantial scatter remaining in the fit suggests that additional as-yet unidentified parameters, or systematic errors in our analysis, affect the data.

The high-density and low-density fits (Table 5, Fig. 19) show interesting differences. The best-fitting exponents on binary fraction have opposite signs, but neither is significant. Density is significant

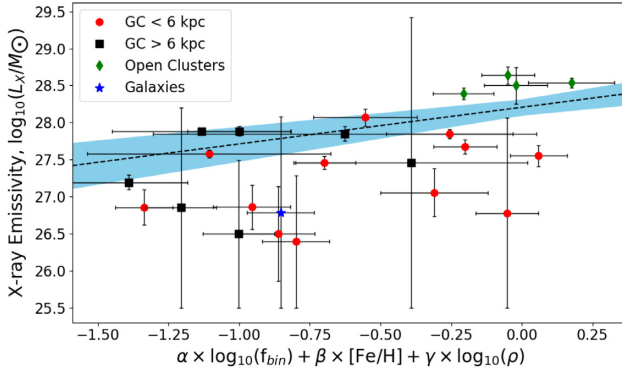


Figure 18. The best-fitting combination of binary fraction, metallicity, and density, plotted versus X-ray emissivity. The exponents used are the best-fitting values of the PyMC3 fit from Table 5, ‘All ρ ’. For the uncertainty description, refer to Figs 13 and 14.

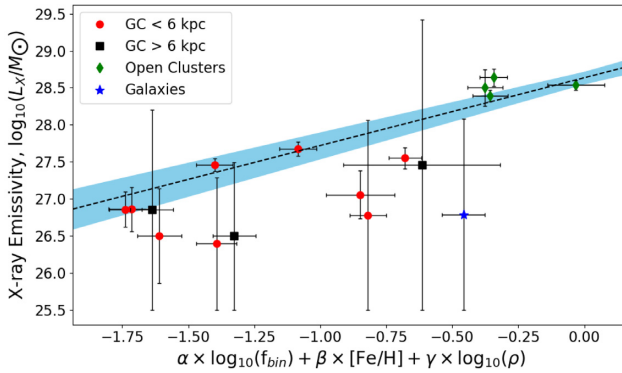


Figure 19. The best-fitting combination of binary fraction, metallicity, and density, plotted versus X-ray emissivity, for low-density populations. The exponents used are the best-fitting values of the PyMC3 fit from Table 5, ‘Low ρ ’. For the uncertainty description, refer to Figs 13 and 14.

(exponent $0.55^{+0.13}_{-0.14}$) for the high-density sample, but not for the low-density sample, while metallicity is the only significant variable for the low-density sample (exponent $1.01^{+0.21}_{-0.24}$). The globular cluster sample does show a significant binary fraction effect, and shows a very strong dependence on density.

We plot the joint distributions of the variables to observe the correlations between variables. Fig. 20 illustrates that there is a strong anticorrelation between the effects of binary fraction (exponent α) and metallicity (exponent β) for the low-density sample, while the effects of density (γ) are not strongly correlated with other parameters.

We also ran bootstrap tests with this paradigm. As described above, our bootstrap tests vary the sample of which objects are included, and randomly locate each data point on the x-coordinate with a probability distribution defined by the error distribution of the data. We generate distributions of the best-fitting values for α , β , γ , and b (the intercept) which we show in Fig. 21 for the low-density sample. As the bootstrap tests remove some of the (already quite small) samples, they substantially increase the errors on the parameters. The bootstrap estimates (Table 6) largely agree with our estimates from the MCMC fitting (see Table 5). In our bootstrap fits to the full sample (‘All ρ ’), we see that only the metallicity exponent remains non-zero at 1σ confidence, while the exponents on binary fraction and age are consistent with zero. The bootstrap

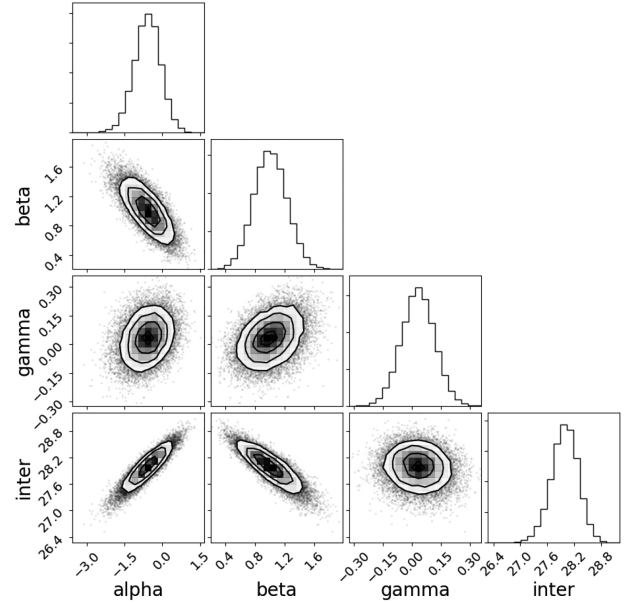


Figure 20. A corner plot (Foreman-Mackey 2016) generated from the ensemble sampling of all populations within the low-density regime. The exponents are with respect to the variables described in Tables 3 and 4: ‘alpha’ on f_{bin} , ‘beta’ on $[{\text{Fe}}/{\text{H}}]$, ‘gamma’ on ρ , and ‘inter’ on L_x/M .

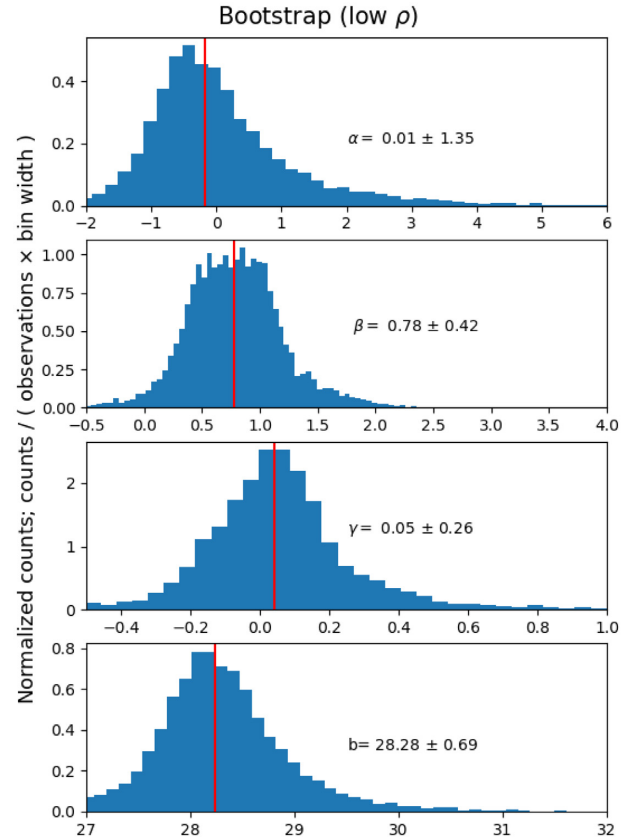


Figure 21. Histograms of the values from our bootstrap test for the exponents α , β , γ on the variables binary fraction, metallicity, and density, as well as the intercept (scale factor) for the low ρ limit. The red line indicates the median of the distribution of each variable, while the mean is written in each panel with its 1σ uncertainty.

Table 6. The best-fitting values and errors (1σ) for the exponent parameters (and intercept) from our bootstrap fits, fitting binary fraction, metallicity, and density. The first column of fits include all our samples, the second include all samples with a density less than $10^4 M_\odot \text{ pc}^{-3}$, the third is all samples with densities above that, while the last column includes only all the globular cluster samples.

Bootstrap	All ρ	Low ρ	High ρ	GCs
α , on f_{bin}	0.08 ± 0.48	0.0 ± 1.4	0 ± 13	0.31 ± 0.39
β , on [Fe/H]	0.33 ± 0.22	0.78 ± 0.42	0.1 ± 6.8	0.11 ± 0.17
γ , on ρ	0.04 ± 0.18	0.04 ± 0.26	0.3 ± 9.2	0.37 ± 0.17
b, on L_X/M	28.2 ± 0.4	28.3 ± 0.7	26 ± 45	26.6 ± 0.4

for the low-density sample also retains a significant exponent for metallicity, while the bootstrap on the high-density sample (the smallest sample) does not constrain any parameter. Finally, the globular cluster sample retains a robust dependence on density in the bootstrap fit.

We conclude that our PyMC3 fits find evidence for a dependence of X-ray emissivity on binary fraction, metallicity, and density, with density having a strong effect at higher densities and metallicity a stronger effect at low densities. However, our robust bootstrap fits suggest substantial degeneracies among these parameters, with only metallicity producing a significant effect for the full and low-density samples, and only density being significant for the globular cluster sample.

5 DISCUSSION

We present a somewhat different perspective than Ge et al. (2015). Ge et al. (2015) carefully compare the X-ray emissivities of four globular clusters with those of several galaxies and open clusters, and argue for the universality of X-ray emissivity in these populations, while we argue that low-density globular clusters have lower X-ray emissivity than open clusters and Galactic populations. Ge et al. (2015) also identify an increased X-ray emissivity of open clusters compared to galactic field populations. We discuss this important point in more detail below, though we confess that we do not yet fully understand the source of this difference.

Key differences between our work and that of Ge et al. (2015) include our use of many more globular clusters, and our identification of a central density above which dynamical formation of X-ray sources substantially enhances the X-ray emissivity. Three of the clusters used by Ge et al. (2015) lie above this density, and we therefore attribute their higher X-ray emissivity to dynamical formation of tight accreting binaries involving WDs or NSs (evidenced by the nature of the X-ray emitting binaries, which are dominated in X-ray flux by neutron stars in 47 Tuc and NGC 6266, and bright CVs in NGC 6397, while in e.g. open clusters chromospherically active binaries dominate). We identify the lower X-ray emissivity of ω Cen as typical of lower density globular clusters, not the exception. Thus, we see a substantial difference in X-ray emissivity between lower density globular clusters and all other populations, including open clusters, that needs explanation. We suggest that binary fraction and/or metallicity may drive this difference.

Recently, Cheng et al. (2018) have assembled a very large sample of *Chandra* observations of globular clusters, and calculated X-ray fluxes for each cluster by extracting spectra from the entire half-mass radius (using an exterior annulus, or other distant regions, for background). This is simpler than the point-source method, allowing them to calculate X-ray emissivities for a larger sample of

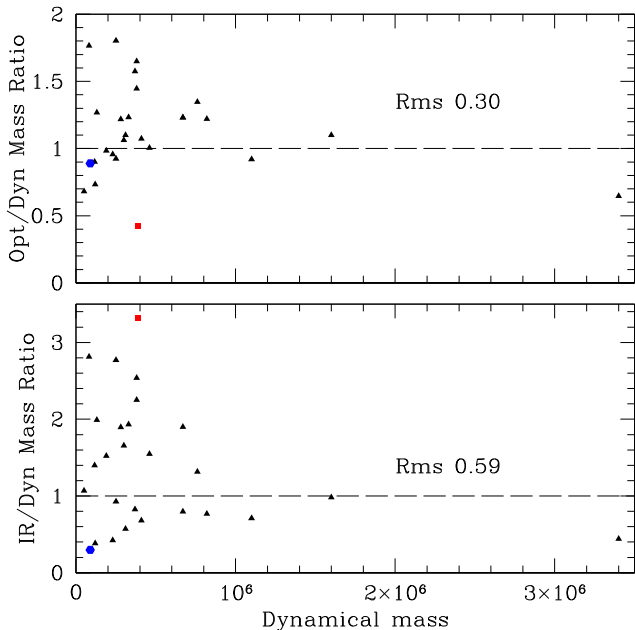


Figure 22. Ratios of dynamical masses of globular clusters (Baumgardt & Hilker 2018) to masses calculated from Harris (1996) (2010 revision) catalogue M_V estimates (top), or by Cheng et al. (2018) using K measurements (bottom). NGC 6397 is indicated with a blue filled hexagon, Terzan 5 by a red square. RMS measurements for both ratios are indicated. The variance is substantially larger when using K measurements.

Galactic globular clusters. Cheng et al. (2018) also find significantly different results; they find a poorer correlation between X-ray emissivity (measured as L_X/L_K) and the stellar interaction rate per unit mass (e.g. their fig. 6), and argue that most GC X-ray sources are primordial binaries, with only a small role for stellar encounter rate. We agree with Cheng et al. that X-ray emission from many GCs (the lower density globular clusters, probably the majority by number) is dominated by primordial binaries, which generally scale with mass. However, there are some complexities with some data sets that may influence their conclusions.

For instance, their fig. 6 (right-hand panel) compares L_X/L_K with γ (stellar encounter rate per unit mass) among 23 well-studied GCs. The correlation here is not as clear as suggested in other works (e.g. Pooley et al. 2003), in large part due to the unusually high values of L_X/L_K adopted for NGC 6397 and NGC 6366. We suggest some systematic errors that may affect their estimates of cluster mass (using K -band estimates) and of L_X .

Cheng et al. (2018) estimate cluster masses using K -band estimates, while we use mass estimates from Baumgardt & Hilker (2018). We compare the spread in the ratio of Cheng et al.'s K -band infrared luminosity estimates to mass, with the spread in the ratio of visible-light luminosity (Harris 1996, 2010 update) to mass, in Fig. 22. Visible-light estimates appear to be superior, as the rms deviations from dynamical mass estimates are 0.30 and 0.59 for visible and K -band estimates, respectively.

Cheng et al. (2018) calculate L_X by extracting all X-ray flux within the half-mass radius. For clusters with high X-ray fluxes, this method works well, but for clusters with low X-ray fluxes (those with few X-ray sources, and/or more distant clusters), it is vulnerable to contamination by fore- or background sources. We suggest that the poorer correlation between normalized encounter rate and normalized L_X in Cheng et al.'s fig. 6 (left-hand panel), versus their fig. 6 (right-hand panel), may be due to their left figure

adding many clusters which are more distant, low-encounter-rate, and/or obscured, and thus adding lower quality data, obscuring the existing correlation.

For instance, as discussed in Section 3.2.1, a background cluster of galaxies is projected on to the low-encounter-rate cluster NGC 6366, producing ~ 75 per cent of the observed X-ray flux within the cluster half-mass radius. We find the X-ray flux from NGC 6366 cluster members to be between 4 and 25 percent of the total flux within its half-mass radius.

In Fig. 23, we show two plots similar to Cheng et al.’s fig. 6 (right-hand panel), plotting normalized encounter rate versus normalized L_X , for the same 23 clusters. On the top, we reproduce Cheng et al.’s plot, and indicate the Pearson and Spearman correlation coefficients. On the bottom, we normalize L_X using dynamical mass estimates (visible-light estimates give similar values) instead of K -band estimates, and rescale the L_X estimate for NGC 6366. The inferred correlation coefficients are significantly higher. This illustrates our argument that careful attention to membership is necessary to get robust measurements of X-ray emissivity, and thus to make these determinations. On the other hand, Cheng et al.’s method is necessary to explore unresolved flux, which is quite important for some cluster observations.

5.1 Metallicity

We find significant evidence for a positive effect of metallicity on the X-ray emissivity of low-luminosity X-ray sources across multiple stellar populations, via multiple tests. The explanation for this is not clear. Most explanations that have been offered to explain the larger numbers of bright LMXBs in higher metallicity globular clusters (e.g. Kim et al. 2013) involve neutron stars or dynamical interactions, which do not seem plausible for the low-density sample. However, Ivanova et al. (2012) identify an increase in the numbers and average masses of red giants in higher metallicity populations. This effect may help explain increased CV and active binary X-ray emission.

5.2 Binary fraction

Verbunt (2001) suggested that the elevated X-ray luminosity per unit mass observed in low-density open clusters could be the result of significant mass-loss (see also van den Berg et al. 2013; Ge et al. 2015; Vats & van den Berg 2017). In the simplest scenario, the total cluster mass is the dominant cluster parameter that decides the number of binaries, with the *primordial* scaling between binary numbers and total cluster mass being roughly linear (e.g. this would arise naturally if the primordial binary fraction is the same in all clusters). The extra rise in X-ray luminosity per unit mass in low-density open clusters seen in Fig. 13 is then due solely to the evaporation of preferentially low-mass *single* stars across the tidal boundary, which inflates the binary fraction. The rate of stellar evaporation is decided by the rate of two-body relaxation, which scales inversely with the total cluster mass. In this scenario, the (observable) binary fraction should reflect this process, and thus one might think the calculation should be straightforward.

However, the binaries that exist in star clusters are limited in orbital period by the density of the cluster, while binaries in the field of galaxies may have much longer orbital periods. The longer orbital period systems found in the field will never interact, and thus do not increase X-ray emissivity. Thus, the details of the binary period distribution, as well as the total binary fraction, will be important in determining X-ray emissivity. The exact details of which binary

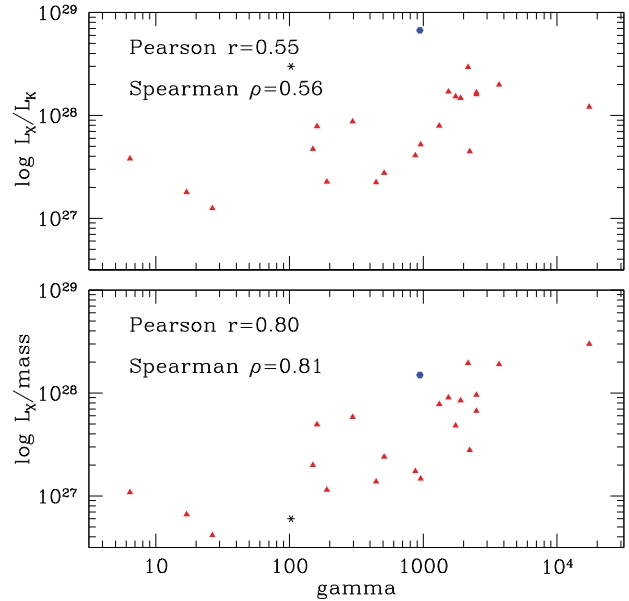


Figure 23. Ratios (y-axis) of L_X to K -band luminosity (Cheng et al. 2018, top), or to masses calculated from visible light Harris (1996, 2010 revision, bottom), compared with the normalized (by mass) stellar interaction rate (x-axis). In the lower panel, we have also adjusted L_X for NGC 6366 (black star), following Section 3. NGC 6397, particularly affected by a spurious K -band luminosity estimate, is indicated with a blue filled hexagon. Pearson and Spearman correlation coefficients are indicated for both samples.

orbital periods contribute efficiently to increasing X-ray emissivity are a complicated topic, beyond the scope of this work.

If the reduced X-ray emissivity of (low-density) globular clusters can be attributed (largely, or wholly) to their reduced binary fraction, this still leaves open the question of why globular clusters have much lower binary fractions than other populations. Binaries of a given orbital period will tend to be disrupted at high densities, and increasing the density destroys binaries of shorter and shorter periods (Heggie 1975). Detailed N -body (Hurley et al. 2007) and Monte Carlo (Fregeau et al. 2009) models of globular clusters indicate that the overall globular cluster binary fraction does not decrease with time in realistic present-day globular clusters, at least when only ‘hard’ binaries (those with short orbital periods – which are also those relevant for X-ray emissivity) are considered. The destruction of binaries in globular cluster cores is counteracted by evaporation of single stars from the outside of the cluster. Including ‘soft’ (long-orbit) binaries can lead to binary fractions that decrease with time, but it appears unlikely that these longer period systems will strongly affect the X-ray emissivity.

A more likely scenario is that most globular clusters were much denser (up to $10^6 M_\odot \text{ pc}^{-3}$ on average within the half-mass radius) during the star formation phase. Such high initial densities, which reduce dramatically as the cluster expands due to gas loss, can substantially reduce cluster binary fractions, especially in those with the largest masses (Sollima 2008; Parker et al. 2009; Marks & Kroupa 2010), as discussed in particular detail by Leigh et al. (2015). There is substantial evidence that blue straggler stars in most clusters are dominated by binaries where one star has transferred mass to the other (Leigh, Sills & Knigge 2007; Knigge, Leigh & Sills 2009; Geller & Mathieu 2011; Gosnell et al. 2015). The numbers of these blue straggler stars generally trace the same decreasing abundance with increasing cluster mass as binary fractions (Piotto et al. 2004; Leigh et al. 2013), indicating that the abundances of

both blue stragglers and X-ray emitting stars in lower density stellar populations may be driven by the fractions of binaries.

6 CONCLUSIONS

In this paper, we investigate the relations between the density, binary fraction, and metallicity of old stellar populations, and their X-ray luminosity per unit mass, or X-ray emissivity. A variety of old populations in galaxies and old clusters show substantially higher L_X/M than low- to moderate-density globular clusters, while the higher density globular clusters show an increase in L_X/M due to well-studied dynamical effects (e.g. Pooley et al. 2003; Bahramian et al. 2013). The substantially higher L_X/M of open clusters compared to most globular clusters was first identified by Verbunt (2001), and subsequently extended to a range of environments (e.g. Revnivtsev et al. 2007; van den Berg et al. 2013; Ge et al. 2015).

In order to investigate X-ray emissivity in different stellar populations, we have compiled a wide range of data from the literature. We identify relatively bright X-ray sources projected on to three low-density environments (the open cluster NGC 6819, the globular cluster NGC 6366, and the Sculptor Dwarf galaxy,) with foreground or background sources, emphasizing the importance of ascertaining membership of X-ray sources among the relevant population.

We show that globular clusters, below a critical density of $\sim 10^4 M_\odot pc^{-3}$, have much lower X-ray emissivities than other populations, while globular clusters above this density have increasing X-ray emissivity with density. At these higher densities, a new population of close binaries is created through dynamical interactions, increasing X-ray emissivity. Comparison of X-ray emissivity with density, age, metallicity, and overall binary fraction suggests that binary fraction and/or metallicity can explain variations in X-ray emissivity in low-density stellar populations, while density has the strongest effect on X-ray emissivity in higher density stellar populations. A straightforward fit to the full sample indicates significant effects from density, metallicity, and binary fraction, but subjecting the fit to bootstrap tests leaves the effect of binary fraction unclear. Further careful study of faint X-ray sources in various stellar populations (in particular, accurate membership of binary fractions in more populations) will elucidate further details of these relations, and test the suggestions here.

ACKNOWLEDGEMENTS

LN thanks M. Mayrand, J. St-Antoine, and the OMM staff for their technical assistance. We acknowledge helpful discussions with R. Arnason, T. Maccarone, and A. Bahramian, and helpful referee reports. COH, GRS, EWR, NI, and LN acknowledge financial support from Discovery Grants from the Natural Sciences and Engineering Research Council (NSERC) of Canada, and COH from a Discovery Accelerator Supplement. LC was supported in part by NASA *Chandra* grant G06-17040X. NI acknowledges support from the CRC program. NWCL acknowledges the generous support of Fondecyt Iniciacion Grant #11180005. AJR is funded by the Australian Research Council through grant number FT170100243. GRS and CLS were supported in part by NASA *Chandra* grants GO7-8078X, GO7-8089A, GO8-9053X, and GO9-9085X, and NASA *Hubble* grants HST-GO-11679.01 and HST-GO-12012.02-A.

The National Radio Astronomy Observatory is a facility of the National Science Foundation (NSF) operated under cooperative agreement by Associated Universities, Inc. Based in part on observations obtained at the Gemini Observatory (and processed using the Gemini IRAF package), which is operated by the Association of Uni-

versities for Research in Astronomy, under a cooperative agreement with the NSF on behalf of the Gemini partnership: the NSF (United States), the National Research Council (Canada), CONICYT (Chile), Ministerio de Ciencia, Tecnología e Innovación Productiva (Argentina), and Ministério da Ciência, Tecnologia e Inovação (Brazil). We acknowledge use of the Hubble Archive at STSci, the *Chandra* Source Catalogue, the NRAO VLA archive, the *Chandra*, *Swift*, and *XMM-Newton* data archives, NASA's Astrophysical Data Service, and arXiv.org, maintained by Cornell University Library. This work has used data from the European Space Agency (ESA) mission *Gaia* (<https://www.cosmos.esa.int/gaia>), processed by the *Gaia* Data Processing and Analysis Consortium (DPAC, <https://www.cosmos.esa.int/web/gaia/dpac/consortium>). Funding for the DPAC has been provided by national institutions, in particular the institutions participating in the *Gaia* Multilateral Agreement.

Code bibliography: XSPEC (Arnaud 1996), CIAO (Fruscione et al. 2006), XMM SAS (<https://www.cosmos.esa.int/web/xmm-newton/sas>), AIPS (<http://www.aips.nrao.edu/index.shtml>), GEMINI IRAF (<https://www.gemini.edu/sciops/data-and-results/processing-software>), PYMC3 (Salvatier et al. 2016), CORNER.PY (Foreman-Mackey 2016), SUPERMONGO (<https://www.astro.princeton.edu/rh1/sm/sm.html>).

REFERENCES

- Agüeros M. A. et al., 2009, *ApJS*, 181, 444
 Anderson J., Cool A. M., King I. R., 2003, *ApJ*, 597, L137
 Anderson J. et al., 2008, *AJ*, 135, 2055
 Arnason R. M., Barmby P., Bahramian A., Maccarone T. J., Zepf S. E., 2019, *MNRAS*, 485, 2259
 Arnaud K. A., 1996, in Jacoby G. H., Barnes J., eds, ASP Conf. Ser. Vol. 101: Astronomical Data Analysis Software and Systems V. Astron. Soc. Pac., San Francisco, p. 17
 Bahramian A., Heinke C. O., Sivakoff G. R., Gladstone J. C., 2013, *ApJ*, 766, 136
 Bahramian A. et al., 2014, *ApJ*, 780, 127
 Balman\$, 2005, *ApJ*, 627, 933
 Bassa C. et al., 2004, *ApJ*, 609, 755
 Bassa C. et al., 2005, *ApJ*, 619, 1189
 Bassa C. G., Pooley D., Verbunt F., Homer L., Anderson S. F., Lewin W. H. G., 2008, *A&A*, 488, 921
 Basu S. et al., 2011, *ApJ*, 729, L10
 Baumgardt H., Hilker M., 2018, *MNRAS*, 478, 1520
 Becker W. et al., 2003, *ApJ*, 594, 798
 Bedin L. R., Salaris M., Piotto G., Cassisi S., Milone A. P., Anderson J., King I. R., 2008, *ApJ*, 679, L29
 Bellazzini M., Fusi Pecci F., Messineo M., Monaco L., Rood R. T., 2002, *AJ*, 123, 1509
 Bellini A. et al., 2010, *A&A*, 513, A50
 Belloni D., Giersz M., Rivera Sandoval L., Askar A., Ciecielag P., 2019, *MNRAS*, 483, 315
 Belloni T., Verbunt F., Mathieu R. D., 1998, *A&A*, 339, 431
 Belloni T., Verbunt F., Schmitt J. H. M. M., 1993, *A&A*, 269, 175
 Bogdanov S., Grindlay J. E., Heinke C. O., Camilo F., Freire P. C. C., Becker W., 2006, *ApJ*, 646, 1104
 Bogdanov S., van den Berg M., Heinke C. O., Cohn H. N., Lugger P. M., Grindlay J. E., 2010, *ApJ*, 709, 241
 Bogdanov S. et al., 2011, *ApJ*, 730, 81
 Bond I. A. et al., 2005, *ApJ*, 620, L103
 Bragaaglia A., Tosi M., 2006, *AJ*, 131, 1544
 Brassington N. J. et al., 2010, *ApJ*, 725, 1805
 Britt C. T. et al., 2013, *ApJ*, 769, 120
 Britt C. T. et al., 2014, *ApJS*, 214, 10
 Brown T. M., Smith E., Ferguson H. C., Rich R. M., Guhathakurta P., Renzini A., Sweigart A. V., Kimble R. A., 2006, *ApJ*, 652, 323
 Campana S., Colpi M., Mereghetti S., Stella L., Tavani M., 1998, *A&AR*, 8, 279

- Carraro G., Villanova S., Demarque P., McSwain M. V., Piotto G., Bedin L. R., 2006, *ApJ*, 643, 1151
 Cheng Z., Li Z., Xu X., Li X., 2018, *ApJ*, 858, 33
 Chumak Y. O., Platais I., McLaughlin D. E., Rastorguev A. S., Chumak O. V., 2010, *MNRAS*, 402, 1841
 Clark G. W., 1975, *ApJ*, 199, L143
 Clark L. L., Sandquist E. L., Bolte M., 2004, *AJ*, 128, 3019
 Coelho P., Mendes de Oliveira C., Cid Fernandes R., 2009, *MNRAS*, 396, 624
 Cohen R. E., Mauro F., Geisler D., Moni Bidin C., Dotter A., Bonatto C., 2014, *AJ*, 148, 18
 Cohn H. N. et al., 2010, *ApJ*, 722, 20
 Cool A. M., Haggard D., Arias T., Brochmann M., Dorfman J., Gafford A., White V., Anderson J., 2013, *ApJ*, 763, 126
 Cox A. N., 2000, Allen's Astrophysical Quantities. Springer, Berlin
 Côté B., Denissenkov P., Herwig F., Ruiter A. J., Ritter C., Pignatari M., Belczynski K., 2018, *ApJ*, 854, 105
 David L. P., Slyz A., Jones C., Forman W., Vrtilek S. D., Arnaud K. A., 1993, *ApJ*, 412, 479
 Davies M. B., 1997, *MNRAS*, 288, 117
 Davis D. S., Richer H. B., Anderson J., Brewer J., Hurley J., Kalirai J. S., Rich R. M., Stetson P. B., 2008, *AJ*, 135, 2155
 De Angeli F., Piotto G., Cassisi S., Busso G., Recio-Blanco A., Salaris M., Aparicio A., Rosenberg A., 2005, *AJ*, 130, 116
 de Boer T. J. L. et al., 2011, *A&A*, 528, A119
 de Marchi F. et al., 2007, *A&A*, 471, 515
 Dempsey R. C., Linsky J. L., Fleming T. A., Schmitt J. H. M. M., 1993, *ApJS*, 86, 599
 Dempsey R. C., Linsky J. L., Fleming T. A., Schmitt J. H. M. M., 1997, *ApJ*, 478, 358
 Dieball A., Long K. S., Knigge C., Thomson G. S., Zurek D. R., 2010, *ApJ*, 710, 332
 Ebeling H., White D. A., Rangarajan F. V. N., 2006, *MNRAS*, 368, 65
 Edmonds P. D., Gilliland R. L., Heinke C. O., Grindlay J. E., 2003, *ApJ*, 596, 1177
 Eger P., Domainko W., Clapson A.-C., 2010, *A&A*, 513, A66
 Elsner R. F. et al., 2008, *ApJ*, 687, 1019
 Fabian A. C., Pringle J. E., Rees M. J., 1975, *MNRAS*, 172, 15P
 Fan X. et al., 1996, *AJ*, 112, 628
 Foreman-Mackey D., 2016, *J. Open Source Softw.*, 1, 24
 Fregeau J. M., Ivanova N., Rasio F. A., 2009, *ApJ*, 707, 1533
 Friel E. D., Janes K. A., Tavarez M., Scott J., Katsanis R., Lotz J., Hong L., Miller N., 2002, *AJ*, 124, 2693
 Fruscione A. et al., 2006, *Proc. SPIE Conf. Ser. Vol. 6270, Observatory Operations: Strategies, Processes, and Systems*. SPIE, Bellingham
 Gaia Collaboration, 2018, *A&A*, 616, A1
 Gaia Collaboration, 2018, *A&A*, 616, A12
 Ge C. et al., 2015, *ApJ*, 812, 130
 Geller A. M., Hurley J. R., Mathieu R. D., 2013, *AJ*, 145, 8
 Geller A. M., Latham D. W., Mathieu R. D., 2015, *AJ*, 150, 97
 Geller A. M., Mathieu R. D., 2011, *Nature*, 478, 356
 Geller A. M., Mathieu R. D., 2012, *AJ*, 144, 54
 Geller A. M., Mathieu R. D., Harris H. C., McClure R. D., 2008, *AJ*, 135, 2264
 Geller A. M. et al., 2017, *ApJ*, 840, 66
 Gendre B., Barret D., Webb N. A., 2003, *A&A*, 400, 521
 Giacconi R. et al., 2001, *ApJ*, 551, 624
 Gondoin P., 2005, *A&A*, 438, 291
 Gosnell N. M., Mathieu R. D., Geller A. M., Sills A., Leigh N., Knigge C., 2015, *ApJ*, 814, 163
 Gosnell N. M., Pooley D., Geller A. M., Kalirai J., Mathieu R. D., Frinchaboy P., Ramirez-Ruiz E., 2012, *ApJ*, 745, 57
 Gozzoli E., Tosi M., Marconi G., Bragaglia A., 1996, *MNRAS*, 283, 66
 Gratton R., Bragaglia A., Carretta E., Tosi M., 2006, *ApJ*, 642, 462
 Grindlay J. E., Heinke C., Edmonds P. D., Murray S. S., 2001, *Science*, 292, 2290
 Grindlay J. E. et al., 2005, *ApJ*, 635, 920
 Grundahl F., Clausen J. V., Hardis S., Frandsen S., 2008, *A&A*, 492, 171
- Guillot S., Rutledge R. E., Bildsten L., Brown E. F., Pavlov G. G., Zavlin V. E., 2009a, *MNRAS*, 392, 665
 Guillot S., Rutledge R. E., Brown E. F., 2011, *ApJ*, 732, 88
 Guillot S., Rutledge R. E., Brown E. F., Pavlov G. G., Zavlin V. E., 2009b, *ApJ*, 699, 1418
 Guillot S., Servillat M., Webb N. A., Rutledge R. E., 2013, *ApJ*, 772, 7
 Göttgens F. et al., 2019, *A&A*, 631, A118
 Güdel M., 2004, *A&AR*, 12, 71
 Güver T., Öznel F., 2009, *MNRAS*, 400, 2050
 Haggard D., Cool A. M., Davies M. B., 2009, *ApJ*, 697, 224
 Hansen B. M. S. et al., 2013, *Nature*, 500, 51
 Harris W. E., 1996, *AJ*, 112, 1487
 Heggie D. C., 1975, *MNRAS*, 173, 729
 Heinke C. O., Grindlay J. E., Edmonds P. D., 2005, *ApJ*, 622, 556
 Heinke C. O., Grindlay J. E., Edmonds P. D., Lloyd D. A., Murray S. S., Cohn H. N., Lugger P. M., 2003b, *ApJ*, 598, 516
 Heinke C. O., Grindlay J. E., Lugger P. M., Cohn H. N., Edmonds P. D., Lloyd D. A., Cool A. M., 2003a, *ApJ*, 598, 501
 Heinke C. O., Rybicki G. B., Narayan R., Grindlay J. E., 2006a, *ApJ*, 644, 1090
 Heinke C. O., Wijnands R., Cohn H. N., Lugger P. M., Grindlay J. E., Pooley D., Lewin W. H. G., 2006b, *ApJ*, 651, 1098
 Hickox R. C., Markevitch M., 2006, *ApJ*, 645, 95
 Hills J. G., 1976, *MNRAS*, 175, 1P
 Hole K. T., Geller A. M., Mathieu R. D., Platais I., Meibom S., Latham D. W., 2009, *AJ*, 138, 159
 Holmberg J., Flynn C., 2000, *MNRAS*, 313, 209
 Hong J., Vesperini E., Belloni D., Giersz M., 2017, *MNRAS*, 464, 2511
 Huang R. H. H., Becker W., Edmonds P. D., Elsner R. F., Heinke C. O., Hsieh B. C., 2010, *A&A*, 513, A16
 Hui C. Y., Cheng K. S., Taam R. E., 2009, *ApJ*, 700, 1233
 Hui C. Y., Cheng K. S., Wang Y., Tam P. H. T., Kong A. K. H., Chernyshov D. O., Dogiel V. A., 2011, *ApJ*, 726, 100
 Hurley J. R., Aarseth S. J., Shara M. M., 2007, *ApJ*, 665, 707
 Hurley J. R., Pols O. R., Aarseth S. J., Tout C. A., 2005, *MNRAS*, 363, 293
 Hut P., Murphy B. W., Verbunt F., 1991, *A&A*, 241, 137
 Idiart T. P., Silík J., de Freitas Pacheco J. A., 2007, *MNRAS*, 381, 1711
 Ivanova N., Belczynski K., Fregeau J. M., Rasio F. A., 2005, *MNRAS*, 358, 572
 Ivanova N., Heinke C. O., Rasio F. A., Taam R. E., Belczynski K., Fregeau J., 2006, *MNRAS*, 372, 1043
 Ivanova N. et al., 2012, *ApJ*, 760, L24
 Jacobson H. R., Pilachowski C. A., Friel E. D., 2011, *AJ*, 142, 59
 Johnston H. M., Kulkarni S. R., Phinney E. S., 1992, in Van Den Heuvel E. P. J., Rappaport S. A., eds, X-Ray Binaries and the Formation of Binary and Millisecond Radio Pulsars. Kluwer, Dordrecht, p. 349
 Johnston H. M., Verbunt F., 1996, *A&A*, 312, 80
 Jonker P. G. et al., 2011, *ApJS*, 194, 18
 Jordán A. et al., 2004, *ApJ*, 613, 279
 Kalirai J. S. et al., 2001, *AJ*, 122, 266
 Kaluzny J., 2003, *Acta Astron.*, 53, 51
 Kaluzny J., Pietrukowicz P., Thompson I. B., Krzeminski W., Schwarzenberg-Czerny A., Pych W., Stachowski G., 2005, *MNRAS*, 359, 677
 Kaluzny J., Stanek K. Z., Garnavich P. M., Challis P., 1997, *ApJ*, 491, 153
 Katz J. I., 1975, *Nature*, 253, 698
 Kiel P. D., Hurley J. R., 2006, *MNRAS*, 369, 1152
 Kim D.-W., Fabbiano G., Ivanova N., Fragos T., Jordán A., Sivakoff G. R., Voss R., 2013, *ApJ*, 764, 98
 Kim D.-W. et al., 2009, *ApJ*, 703, 829
 Knigge C., Leigh N., Sills A., 2009, *Nature*, 457, 288
 Kobulnicky H. A. et al., 2005, *AJ*, 129, 239
 Kong A. K. H., Bassa C., Pooley D., Lewin W. H. G., Homer L., Verbunt F., Anderson S. F., Margon B., 2006, *ApJ*, 647, 1065
 Kroupa P., Aarseth S., Hurley J., 2001, *MNRAS*, 321, 699
 Kundu A., Maccarone T. J., Zepf S. E., Puzia T. H., 2003, *ApJ*, 589, L81
 Lan S.-H., Kong A. K. H., Verbunt F., Lewin W. H. G., Bassa C., Anderson S. F., Pooley D., 2010, *ApJ*, 712, 380
 Lanzoni B. et al., 2010, *ApJ*, 717, 653

- Lee-Brown D. B., Anthony-Twarog B. J., Deliyannis C. P., Rich E., Twarog B. A., 2015, *AJ*, 149, 121
- Leigh N., Knigge C., Sills A., Perets H. B., Sarajedini A., Glebbeek E., 2013, *MNRAS*, 428, 897
- Leigh N., Sills A., Knigge C., 2007, *ApJ*, 661, 210
- Leigh N. W. C., Geller A. M., 2013, *MNRAS*, 432, 2474
- Leigh N. W. C., Giersz M., Marks M., Webb J. J., Hypki A., Heinke C. O., Kroupa P., Sills A., 2015, *MNRAS*, 446, 226
- Liedahl D. A., Osterheld A. L., Goldstein W. H., 1995, *ApJ*, 438, L115
- Liu Q. Z., van Paradijs J., van den Heuvel E. P. J., 2007, *A&A*, 469, 807
- Lorimer D. R. et al., 2015, *MNRAS*, 450, 2185
- Lugger P. M., Cohn H. N., Heinke C. O., Grindlay J. E., Edmonds P. D., 2007, *ApJ*, 657, 286
- Lu T.-N., Kong A. K. H., Bassa C., Verbunt F., Lewin W. H. G., Anderson S. F., Pooley D., 2009, *ApJ*, 705, 175
- Lu T.-N., Kong A. K. H., Verbunt F., Lewin W. H. G., Anderson S. F., Pooley D., 2011, *ApJ*, 736, 158
- Lynch R. S., Ransom S. M., 2011, *ApJ*, 730, L11
- Maccarone T. J., Kundu A., Zepf S. E., Piro A. L., Bildsten L., 2005, *MNRAS*, 364, L61
- Maccarone T. J. et al., 2012, *MNRAS*, 426, 3057
- Mapelli M., Ripamonti E., Battaglia G., Tolstoy E., Irwin M. J., Moore B., Sigurdsson S., 2009, *MNRAS*, 396, 1771
- Marks M., Kroupa P., 2010, *MNRAS*, 406, 2000
- Marín-Franch A. et al., 2009, *ApJ*, 694, 1498
- Mateo M. L., 1998, *ARA&A*, 36, 435
- Maxwell J. E., Lugger P. M., Cohn H. N., Heinke C. O., Grindlay J. E., Budac S. A., Drukier G. A., Bailyn C. D., 2012, *ApJ*, 756, 147
- Mazure A., Capelato H. V., 2002, *A&A*, 383, 384
- McConnachie A. W., 2012, *AJ*, 144, 4
- McLaughlin D. E., van der Marel R. P., 2005, *ApJS*, 161, 304
- Meibom S. et al., 2009, *AJ*, 137, 5086
- Milliman K. E., Mathieu R. D., Geller A. M., Gosnell N. M., Meibom S., Platais I., 2014, *AJ*, 148, 38
- Milone A. P., Piotti G., Bedin L. R., Sarajedini A., 2008, *Mem. Soc. Astron. Ital.*, 79, 623
- Milone A. P. et al., 2012, *A&A*, 540, A16
- Monachesi A., Trager S. C., Lauer T. R., Hidalgo S. L., Freedman W., Dressler A., Grillmair C., Michell K. J., 2012, *ApJ*, 745, 97
- Monkiewicz J. et al., 1999, *PASP*, 111, 1392
- Mushotzky R. F., Cowie L. L., Barger A. J., Arnaud K. A., 2000, *Nature*, 404, 459
- Nardiello D. et al., 2018, *MNRAS*, 481, 3382
- Nordström B. et al., 2004, *A&A*, 418, 989
- Nucita A. A., de Paolis F., Ingrosso G., Carpano S., Guainazzi M., 2008, *A&A*, 478, 763
- O’Malley E. M., Gilligan C., Chaboyer B., 2017, *ApJ*, 838, 162
- Parker R. J., Goodwin S. P., Kroupa P., Kouwenhoven M. B. N., 2009, *MNRAS*, 397, 1577
- Patterson J., 1998, *PASP*, 110, 1132
- Pecaut M. J., Mamajek E. E., 2013, *ApJS*, 208, 9
- Pecaut M. J., Mamajek E. E., Bubar E. J., 2012, *ApJ*, 746, 154
- Pfahl E., Rappaport S., Podsiadlowski P., 2003, *ApJ*, 597, 1036
- Pfahl E., Rappaport S., Podsiadlowski P., Spruit H., 2002, *ApJ*, 574, 364
- Pietrzyński G. et al., 2008, *AJ*, 135, 1993
- Piotti G. et al., 2004, *ApJ*, 604, L109
- Platais I., Cudworth K. M., Kozhurina-Platais V., McLaughlin D. E., Meibom S., Veillet C., 2011, *ApJ*, 733, L1
- Platais I., Gosnell N. M., Meibom S., Kozhurina-Platais V., Bellini A., Veillet C., Burkhead M. S., 2013, *AJ*, 146, 43
- Pooley D., Hut P., 2006, *ApJ*, 646, L143
- Pooley D. et al., 2002a, *ApJ*, 569, 405
- Pooley D. et al., 2002b, *ApJ*, 573, 184
- Pooley D. et al., 2003, *ApJ*, 591, L131
- Prager B. J., Ransom S. M., Freire P. C. C., Hessels J. W. T., Stairs I. H., Arras P., Cadelano M., 2017, *ApJ*, 845, 148
- Pretorius M. L., Knigge C., O’Donoghue D., Henry J. P., Gioia I. M., Mullis C. R., 2007, *MNRAS*, 382, 1279
- Queloz D., Dubath P., Pasquini L., 1995, *A&A*, 300, 31
- Raghavan D. et al., 2010, *ApJS*, 190, 1
- Ramsay G., Wu K., 2006, *A&A*, 447, 199
- Randich S., 1997, *Mem. Soc. Astron. Ital.*, 68, 971
- Ransom S. M., Hessels J. W. T., Stairs I. H., Freire P. C. C., Camilo F., Kaspi V. M., Kaplan D. L., 2005, *Science*, 307, 892
- Revnivtsev M., Churazov E., Sazonov S., Forman W., Jones C., 2007, *A&A*, 473, 783
- Revnivtsev M., Churazov E., Sazonov S., Forman W., Jones C., 2008, *A&A*, 490, 37
- Roeser S., Demleitner M., Schilbach E., 2010, *AJ*, 139, 2440
- Rutledge G. A., Hesser J. E., Stetson P. B., Mateo M., Simard L., Bolte M., Friel E. D., Copin Y., 1997, *PASP*, 109, 883
- Saeedi S., Sasaki M., Ducci L., 2018, *MNRAS*, 473, 440
- Salaris M., Weiss A., 2002, *A&A*, 388, 492
- Salvatier J., Wiecki T., Fonnesbeck C., 2016, *PeerJ Comput. Sci.*, 2, e55
- Saracini C. L., Kundu A., Irwin J. A., Sivakoff G. R., Blanton E. L., Randall S. W., 2003, *ApJ*, 595, 743
- Sazonov S., Revnivtsev M., Gilfanov M., Churazov E., Sunyaev R., 2006, *A&A*, 450, 117
- Schweitzer A. E., Cudworth K. M., Majewski S. R., Suntzeff N. B., 1995, *AJ*, 110, 2747
- Schwpoje A. D., Brunner H., Buckley D., Greiner J., Heyden K. v. d., Neizvestny S., Potter S., Schwarz R., 2002, *A&A*, 396, 895
- Servillat M., Webb N. A., Barret D., 2008a, *A&A*, 480, 397
- Servillat M. et al., 2008b, *A&A*, 490, 641
- Shara M. M., Hurley J. R., 2006, *ApJ*, 646, 464
- Shishkovsky L. et al., 2018, *ApJ*, 855, 55
- Silva D. R., Cornell M. E., 1992, *ApJS*, 81, 865
- Sivakoff G. R. et al., 2007, *ApJ*, 660, 1246
- Skrutskie M. F. et al., 2006, *AJ*, 131, 1163
- Sollima A., 2008, *MNRAS*, 388, 307
- Sollima A., Beccari G., Ferraro F. R., Fusi Pecci F., Sarajedini A., 2007, *MNRAS*, 380, 781
- Sollima A., Carballo-Bello J. A., Beccari G., Ferraro F. R., Pecci F. F., Lanzoni B., 2010, *MNRAS*, 401, 577
- Sommarriva V., Piotti G., Rejkuba M., Bedin L. R., Heggie D. C., Mathieu R. D., Villanova S., 2009, *A&A*, 493, 947
- Sonbas E., Rangelov B., Kargaltsev O., Dhuga K. S., Hare J., Volkov I., 2016, *ApJ*, 821, 54
- Stehle R., Kolb U., Ritter H., 1997, *A&A*, 320, 136
- Stelzer B., Marino A., Micela G., López-Santiago J., Liefke C., 2013, *MNRAS*, 431, 2063
- Strader J., Caldwell N., Seth A. C., 2011, *AJ*, 142, 8
- Trager S., Djorgovski S., King I., 1993, in Djorgovski S., Meylan G., eds, *ASP Conf. Ser. Vol. 50, Structure and Dynamics of Globular Clusters*. Astron. Soc. Pac., San Francisco, p. 347
- Trinchieri G. et al., 2008, *ApJ*, 688, 1000
- Vaiana G. S., 1983, in Stenflo J. O., ed., *Proc. IAU Symp. 102, Solar and Stellar Magnetic Fields: Origins and Coronal Effects*. D. Reidel Publishing Company, Dordrecht, p. 165
- Valenti E., Ferraro F. R., Origlia L., 2007, *AJ*, 133, 1287
- VandenBerg D. A., Brogaard K., Leaman R., Casagrande L., 2013, *ApJ*, 775, 134
- van den Berg M., Stassun K. G., Verbunt F., Mathieu R. D., 2002, *A&A*, 382, 888
- van den Berg M., Tagliaferri G., Belloni T., Verbunt F., 2004, *A&A*, 418, 509
- van den Berg M., Verbunt F., Tagliaferri G., Belloni T., Bedin L. R., Platais I., 2013, *ApJ*, 770, 98
- van Dokkum P. G., 2001, *PASP*, 113, 1420
- Vats S., van den Berg M., 2017, *ApJ*, 837, 130
- Vats S., van den Berg M., Wijnands R., 2018, *MNRAS*, 481, 3708
- Verbunt F., 1987, *ApJ*, 312, L23
- Verbunt F., 2000, in Pallavicini R., Micela G., Sciotino S., eds, *Proc. IAU Symp. 198, Stellar Clusters and Associations: Convection, Rotation, and Dynamos*. Int. Astron. Un., Paris, p. 421
- Verbunt F., 2001, *A&A*, 368, 137

- Verbunt F, 2003, in Piotto G., Meylan G., Djorgovski S. G., Riello M., eds, ASP Conf. Ser. Vol. 296, New Horizons in Globular Cluster Astronomy. Astron. Soc. Pac., San Francisco, p. 245
- Verbunt F, Hut P, 1987, in Helfand D. J., Huang J.-H., eds, Proc. IAU Symp. 125: The Origin and Evolution of Neutron Stars. Springer, Berlin, p. 187
- Verbunt F, Pooley D., Bassa C., 2008, in Vesperini E., Giersz M., Sills A., eds, Proc. IAU Symp. 246, *Dynamical Evolution of Dense Stellar Systems*. Cambridge Univ. Press, Cambridge , p. 301
- Verbunt F, van Kerkwijk M. H., in't Zand J. J. M., Heise J., 2000, A&A, 359, 960
- Verbunt F, van Paradijs J., Elson R., 1984, MNRAS, 210, 899
- Warwick R. S., 2014, MNRAS, 445, 66
- Watkins L. L., van der Marel R. P., Bellini A., Anderson J., 2015, ApJ, 812, 149
- Webb N. A., Servillat M., 2013, A&A, 551, A60
- Webb N. A., Wheatley P. J., Barret D., 2006, A&A, 445, 155
- Wilms J., Reynolds C. S., Begelman M. C., Reeves J., Molendi S., Staubert R., Kendziorra E., 2001, MNRAS, 328, L27
- Wu E. M. H., Hui C. Y., Kong A. K. H., Tam P. H. T., Cheng K. S., Dogiel V. A., 2014, ApJ, 788, L40
- Yuasa T., Nakazawa K., Makishima K., 2009, PASJ, 61, 1107
- Zhao B., Bailyn C. D., 2005, AJ, 129, 1934

APPENDIX A: DETAILS ON INDIVIDUAL GLOBULAR CLUSTERS

NGC 3201: Webb et al. (2006) report an *XMM* observation of NGC 3201, with four sources located within the half-mass radius, though not concentrated in the core. An archival Chandra observation of NGC 3201 (ObsID 11031) finds 22 sources projected within the half-mass radius of the cluster with total $L_X(0.5\text{--}2 \text{ keV})$ (assuming the cluster N_{H} and a power law of photon index 2) of $1.3 \times 10^{32} \text{ erg s}^{-1}$, though all could be background sources. Cheng et al. (2018) measure the total X-ray flux from NGC 3201 to be $<7.5 \times 10^{31} \text{ erg s}^{-1}$ (correcting to the 0.5–2 keV band using their choice of a $\Gamma = 2$ power-law), consistent with our analysis.

NGC 4372: An *XMM* observation of NGC 4372 reported by Servillat et al. (2008a) reported no X-ray sources within the half-mass radius. A recent archival Chandra observation (PI Chomiuk) reveals six faint sources within NGC 4372’s half-mass radius. Assuming a power-law of photon index 1.8, with the cluster N_{H} , gives an estimate of $L_X = 1.2 \times 10^{32} \text{ erg s}^{-1}$ for their luminosity, though it is unclear whether any of these X-ray sources are associated with the cluster. Using the ‘double-subtraction’ method to analyse the total emission from the half-mass radius, we measure the X-ray flux from NGC 4372 to be $<1.8 \times 10^{31} \text{ erg s}^{-1}$, consistent with our point-source analysis.

ω Cen/NGC 5139: For ω Cen, we use a half-mass radius of 5 arcmin (following the 2010 revision of the Harris catalogue), and accept the optical identifications of cluster members listed in Cool et al. (2013) within that radius, to determine the minimum L_X from the cluster ($L_{X,\min}(0.5\text{--}2 \text{ keV}) = 5.7 \times 10^{32} \text{ erg s}^{-1}$). The Cheng et al. (2018) estimate of the total 0.5–2 keV L_X is $7.1 \times 10^{32} \text{ erg s}^{-1}$, which is basically consistent.

M12/NGC 6218: For M12, we accept the identification of the X-ray source CX1 as a secure cluster member by Lu et al. (2009), supported by Göttgens et al. (2019). We use the *HST* proper motion catalogue of Nardiello et al. (2018) to check the membership status of the other sources. We find that the star CX2b (a sub-subgiant) is not a cluster member, while CX2c (a candidate CV) is a cluster member, and verify its blue colours in the ultraviolet. We confirm CX2 as a CV and cluster member, but are not able to ascertain membership for sources CX3-6. We obtain

$L_{X,\min} = 9 \times 10^{31} \text{ erg s}^{-1}$, while the Cheng et al. (2018) total L_X estimate is $1.4 \times 10^{32} \text{ erg s}^{-1}$.

M10/NGC 6254: NGC 6254/M10 has one secure cluster member X-ray source reported so far, the radio source reported by Shishkovsky et al. (2018), with $L_X(0.5\text{--}2) = 7.3 \times 10^{30} \text{ erg s}^{-1}$. We identify a further 10 sources in M10, spread across the half-mass radius, giving a maximum point source $L_{X,\max}(0.5\text{--}2) = 1.3 \times 10^{32} \text{ erg s}^{-1}$. We also perform a double-subtraction spectral analysis of the Chandra data within the half-mass radius, finding $L_X(0.5\text{--}2) = 6.9 \pm 2.5 \times 10^{31} \text{ erg s}^{-1}$.

NGC 6304: We use the 97 ks Chandra observation of NGC 6304 (Guillot et al. 2013), and find 17 X-ray sources within the half-mass radius between 0.5 and 2 keV, concentrated towards the cluster core. The brightest of these is the quiescent LMXB reported by Guillot et al. (2009a,b), which has a 0.5–2 keV L_X of $6.1 \times 10^{32} \text{ erg s}^{-1}$ (from a direct spectral fit using an absorbed NSATMOS hydrogen atmosphere neutron star model). Including the other detected point sources gives $L_X = 8.1 \times 10^{32} \text{ erg s}^{-1}$. However, Cheng et al. (2018) measure $1.45^{+0.08}_{-0.05} \times 10^{33} \text{ erg s}^{-1}$ (corrected to 0.5–2 keV) using all Chandra data within the half-mass radius. Our own measurement of the total L_X within the half-mass radius for this cluster gives $1.2^{+0.4}_{-0.3} \times 10^{33} \text{ erg s}^{-1}$, between the other two estimates.

Guillot et al. (2009a) suggested that two X-ray sources lying outside the cluster half-mass radius, XMMU 171411-293159 and XMMU 171421-292917, are cluster members and quiescent LMXBs, and showed that they are clearly associated with the stars 2MASS 17141152-2931594 and 2MASS 17142095-2929163. However, these stars now have *Gaia* parallax distances ($800 \pm 100 \text{ pc}$; $732 \pm 20 \text{ pc}$) and proper motions ($\text{pmRA} = -3.79 \pm 0.09 \text{ mas yr}^{-1}$, $\text{pmDec} = -5.93 \pm 0.06 \text{ mas yr}^{-1}$; and $\text{pmRA} = 0.81 \pm 0.07 \text{ mas yr}^{-1}$, $\text{pmDec} = -2.15 \pm 0.04 \text{ mas yr}^{-1}$) inconsistent with the distance (5.9 kpc) and *Gaia* Collaboration (2018) proper motion ($\text{pmRA} = -3.95 \pm 0.01 \text{ mas yr}^{-1}$, $\text{pmDec} = -1.125 \pm 0.007 \text{ mas yr}^{-1}$) of NGC 6304, so are clearly not members of NGC 6304.

NGC 6352: We analyse an archival 19.8 ks *Chandra* observation of NGC 6352 (ObsID 13674), finding ten likely X-ray sources in the cluster, the membership of which are uncertain (they are not clustered in the core). We find a total possible point source luminosity of $L_X = 1.8 \times 10^{32} \text{ erg s}^{-1}$, while Cheng et al. (2018) measure a total of $L_X = 3.5 \pm 0.7 \times 10^{32} \text{ erg s}^{-1}$.

NGC 6366: The unusual extended X-ray source CX1b in NGC 6366 (Bassa et al. 2008) is discussed in detail in Section 3.2 below, where it is shown to be a background cluster of galaxies. In Section 3.2, we present evidence that the giant star associated with CX1a is the correct optical counterpart and is associated with the cluster.

The half-mass radius of 2.92 arcmin of NGC 6366 also includes CX2, CX3, CX4, CX5, and CX14 (note that Bassa et al. 2008 used a smaller half-mass radius, leaving CX14 outside). Of these, we can verify only CX5 as a cluster member; the optical counterpart has a proper motion, measured with both *HST* (using the ACS and WFC3 surveys; Nardiello et al. 2018) and *Gaia*, consistent with the cluster proper motion, indicating cluster membership. CX5’s counterpart is a sub-subgiant in the CMD; as the fraction of sub-subgiants that are X-ray sources is quite large (Geller et al. 2017), we consider it very likely that this star is the true counterpart to CX5. The other sources we take to be possible members, giving us a point source $L_X = 1.4 \times 10^{31} - 3.1 \times 10^{31} \text{ erg s}^{-1}$. Cheng et al. (2018) measure $L_X(0.5\text{--}2) = 1.5 \pm 0.5 \times 10^{32} \text{ erg s}^{-1}$. We double check this measurement using the double subtraction method, and measure $L_X(0.5\text{--}2) = 1.2^{+0.4}_{-0.6} \times 10^{32} \text{ erg s}^{-1}$. However, this includes

a background cluster of galaxies; subtracting its flux ($L_X = 6 \times 10^{31}$ if it were in NGC 6366) leaves us with only an upper limit of $L_X(0.5-2) < 6 \times 10^{31} \text{ erg s}^{-1}$, consistent with the point source measurement.

NGC 6388: We use the *XMM* flux measurement of NGC 6388 from Nucita et al. (2008), which is consistent with the *Chandra* estimate (Maxwell et al. 2012), as the *XMM* flux includes all the X-ray emission from the core of this rich cluster.

NGC 6544: Significant background flaring occurred during the 16.5 ks *Chandra* observation of NGC 6544 (ObsID 5435); removing this leaves 12 ks. Five clear sources can be seen within the half-mass radius, plus diffuse emission concentrated within a couple arcsec of the cluster centre location of Cohen et al. (2014). Since the total X-ray flux substantially exceeds the expected cosmic background, we estimate the X-ray luminosity of the cluster by subtracting the latter. The Harris (1996, 2010 edition) catalogue reports NGC 6544 as the cluster with the highest central density, $10^{6.06} \text{ L}_\odot \text{ pc}^{-3}$. However, Cohen et al. (2014) report a new photometric and structural study of NGC 6544 that gives a larger core and lower central density, which we calculate to be $10^{5.45} \text{ L}_\odot \text{ pc}^{-3}$. Cheng et al. (2018) give a total luminosity, $L_X(0.5-2) = 9 \pm 2 \times 10^{31} \text{ erg s}^{-1}$, about twice our estimated point source luminosity $L_X = 4.7 \times 10^{31} \text{ erg s}^{-1}$.

NGC 6553: Guillot et al. (2011) report *XMM* and *Chandra* observations of NGC 6553, identifying 21 X-ray sources within the half-mass radius. They identify one secure cluster member (a qLMXB, their source 3), and show that one source (#5) is not a member. We calculate the 0.5–2 keV minimum unabsorbed flux from their spectral fit to source #3. For other objects within the half-mass radius, we are not able to reproduce the fluxes listed in their table 2 from their count rates and reported spectral models, so we instead calculate fluxes assuming a power law of photon index 2, from the pn count rates provided by Guillot et al., and checked using an independent analysis of the longer *Chandra* observation, finding a total point source $L_X = 4.7 \times 10^{32} \text{ erg s}^{-1}$. Cheng et al. (2018) measure a flux from the half-mass radius of $7.7 \times 10^{32} \text{ erg s}^{-1}$.

M28/NGC 6626: We used the longest (142 ks) *Chandra* exposure of M28 (Bogdanov et al. 2011), and detected 66 sources in the 0.5–2 keV range. These gave a maximum point source $L_X = 2.57 \times 10^{33} \text{ erg s}^{-1}$, in good agreement with the total flux estimate from Cheng et al. (2018) of $L_X(0.5-2) = 2.88 \times 10^{33} \text{ erg s}^{-1}$.

M22/NGC 6656: Webb & Servillat (2013) report 15 X-ray sources detected by *Chandra* within M22's half-mass radius. We regard only the optically identified CV1 (Anderson, Cool & King 2003; Bond et al. 2005; Webb & Servillat 2013) and the millisecond pulsar PSR J1836-2354A (Lynch & Ransom 2011; Webb & Servillat 2013) as verified cluster sources, giving a minimum $L_X(0.5-2) = 7.6 \times 10^{31} \text{ erg s}^{-1}$, and a maximum of $2.9 \times 10^{32} \text{ erg s}^{-1}$. Cheng et al. (2018) give an intermediate estimate of the flux within the half-mass radius of $1.8 \times 10^{32} \text{ erg s}^{-1}$.

M55/NGC 6809: M55 has one CV (CX1) that has shown a recorded outburst (Kaluzny et al. 2005), and one source (CX7) with an optical counterpart located in the sub-subgiant region, where spurious matches are very rare (Bassa et al. 2008). Bassa et al.'s optical counterpart to CX7 is present in *Gaia* DR2, and its proper motion is consistent with NGC 6809's proper motion (*Gaia* Collaboration 2018). We take CX1 and CX7 to be secure cluster members, giving a minimum $L_X = 4 \times 10^{31} \text{ erg s}^{-1}$ and a maximum of $1.2 \times 10^{32} \text{ erg s}^{-1}$. Cheng et al. (2018) gives a limit on the total flux from the half-mass radius of $6 \times 10^{31} \text{ erg s}^{-1}$.

M71/NGC 6838: Huang et al. (2010) presented a detailed search for optical counterparts in M71. We regard the following as secure

cluster members: s08 (radio-detected millisecond pulsar), s04, s06, s07, s18, s20, s27a (giant, subgiant, or sub-subgiant stars with proper motions reported by Nardiello et al. 2018 and *Gaia* DR2 that agree with the *Gaia* Collaboration 2018 cluster proper motion), s19a (sub-subgiant, proper motion verified by *HST*; Nardiello et al. 2018), and s29 (CV, identified by strong UV excess versus redder $V-I$ colours). We exclude the foreground sources s02, s12, s16, s22, s24, and s26; we confirm that the *HST* proper motions of the first four are discordant with the cluster motion. The X-ray point source luminosity associated with the cluster is then in the range of $L_X = 5.9 \times 10^{31}-1.4 \times 10^{32} \text{ erg s}^{-1}$, consistent with the total luminosity estimate of $1.3 \times 10^{32} \text{ erg s}^{-1}$ of Cheng et al. (2018).

E3 and NGC 6144: No X-ray sources projected on the globular clusters E3 or NGC 6144 (Lan et al. 2010) can be confidently identified as members of their clusters. E3 CX03 is identified by Lan et al. as a background galaxy. We identify a $G = 15$ *Gaia* (*Gaia* Collaboration 2018) source with a parallax distance of $553 \pm 15 \text{ pc}$ (thus a clear foreground source) with E3 CX01, leaving only E3 CX02 ($L_X = 2.8 \times 10^{31} \text{ erg s}^{-1}$) as a candidate cluster member. Extracting the total flux from E3's half-mass radius gives a total $L_X(0.5-2) = 3.7 \pm 1.2 \times 10^{32} \text{ erg s}^{-1}$, substantially larger than the resolved source measurement.

For NGC 6144, the suggested counterparts to CX1 and CX2 (Lan et al. 2010) show blue colours in UV *HST* filters (supporting a CV nature), but Nardiello et al. (2018) cannot estimate their membership probability, so we are not certain they are not AGN. Cheng et al. (2018) estimate a total half-mass flux of $4.2 \times 10^{32} \text{ erg s}^{-1}$.

Palomar 6, Palomar 10, IC 1276: No X-ray sources are detected within the half-mass radii of Palomar 10 (ObsID 8945), Palomar 6 (ObsIDs 9986 and 10010), or IC 1276 (observed only by *Swift*). We set upper limits for these using the total possible excess X-ray counts within the half-mass radius of each cluster. Cheng et al. (2018) give an upper limit of $L_X < 1.8 \times 10^{32} \text{ erg s}^{-1}$ for Palomar 10. We estimate an upper limit of $L_X < 6.8 \times 10^{31} \text{ erg s}^{-1}$ for Palomar 6 from *Chandra* ObsID 10010, and an upper limit of $L_X < 8 \times 10^{31} \text{ erg s}^{-1}$ for IC 1276 from a 2.4 ksec *Swift/XRT* observation.

¹Department of Physics, University of Alberta, CCIS 4-183, Edmonton, AB T6G 2E1, Canada

²Department of Physics and Astronomy, Michigan State University, East Lansing, MI 48824, USA

³Department of Astronomy, Indiana University, 727 E. Third Street, Bloomington, IN 47405, USA

⁴Department of Physics, University of Surrey, Guildford GU2 7XH, UK

⁵Institute of Astronomy, National Tsing Hua University, Hsinchu 30013, Taiwan

⁶Department of Astrophysics, American Museum of Natural History, Central Park West and 79th Street, New York, NY 10024-5192, USA

⁷Departamento de Astronomía, Facultad de Ciencias Físicas y Matemáticas, Universidad de Concepción, Concepción, Chile

⁸Department of Physics and Astronomy, Bishop's University, 2600 rue College, Sherbrooke, Québec J1M 1Z7, Canada

⁹School of Physical, Environmental and Mathematical Sciences, University of New South Wales, Australian Defence Force Academy, Canberra, ACT 2600, Australia

¹⁰Department of Astronomy, University of Virginia, PO Box 400325, Charlottesville, VA 22904, USA

¹¹Department of Physics, University of Nevada, Reno, NV 89557, USA

¹²Harvard-Smithsonian Center for Astrophysics, 60 Garden Street, Cambridge, MA 02138, USA